# ATLAS CSC NOTE

ATL-PHYS-PUB-2008-xxx

March 24, 2008

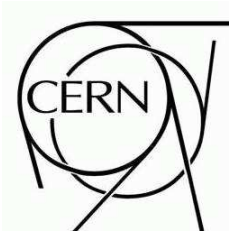


## Diboson Physics Studies With the ATLAS Detector

The ATLAS Collaboration[1)]

### Abstract

This note presents studies of the sensitivity of the ATLAS experiment to Standard Model diboson ($W^+W^-$, $W^\pm Z$, $ZZ$, $W^\pm\gamma$, and $Z\gamma$) production in pp collisions at $\sqrt{s} = 14$ TeV, using final states containing electrons, muons and photons. The studies use the ATLAS Computer System Commissioning (CSC) Monte Carlo datasets, which include trigger information and detector calibration and alignment corrections. The influence of backgrounds on diboson detection is assessed using large samples of fully simulated background events. The cross section measurement uncertainties (both statistical and systematic) are estimated as a function of integrated luminosity (from 0.1 to 30 fb$^{-1}$). The studies show that the Standard Model $W^+W^-$, $W^\pm Z$, $W^\pm\gamma$, and $Z\gamma$ signals can be established with statistical sensitivity better than $5\sigma$ for the first 0.1 fb$^{-1}$ of integrated luminosity, and the $ZZ$ signal can be established with 1.0 fb$^{-1}$ of integrated luminosity. The ATLAS experiment's sensitivity to anomalous triple gauge boson couplings is also established. The anomalous triple gauge boson coupling sensitivities can be significantly improved, even with 0.1 fb$^{-1}$ of data, over the results from the Tevatron that use 1.0 fb$^{-1}$ of data.

*This note is part of XXXX. This version of the note should not be cited: all citations should be to XXXX.*

[1)]This note prepared by Tom Barber, Richard Batley, Andrea Bocci, John Chapman, Electra Christidi, Tiesheng Dai, Al Goshaw, Liang Han, Chris Hays, Suen Hou, Yi Jiang, Bachas Konstantinos, Ashutosh Kotwal, Mark Kruse, Dan Levin, Xuefei Li, Zhijun Liang, Hong Ma, Chara Petridou, Dragan Popović, Dimos Sampsonidis, Ljiliana Simić, Nenad Vranješ, Pat Ward, Alan Wilson, Haijun Yang, Yi Yang, Pei Zhang, Zhengguo Zhao, Jiahang Zhong, and Bing Zhou

# Contents

# 1 Introduction

This paper presents studies of the ATLAS experiment's sensitivity to diboson ($W^+W^-$, $W^\pm Z$, $ZZ$, $W^\pm\gamma$, $Z\gamma$) production using lepton and photon final states, and the corresponding ability to set limits on triple gauge boson couplings (TGC). Results are based on Monte Carlo datasets produced in the ATLAS Computing System Commissioning (CSC) program. The analysis of diboson production at the LHC provides an important test of the high energy behavior of electroweak interactions. Vector boson self-couplings are fundamental predictions of the Standard Model (SM) [1], resulting from the non-Abelian nature of the $SU(2)_L \times U(1)_Y$ gauge symmetry theory.

Any theory predicting physics beyond the Standard Model while maintaining the Standard Model as a low-energy limit may introduce deviations in the gauge couplings at some high energy scale. Precise measurements of the couplings will not only provide stringent tests of the Standard Model, but will also probe for new physics in the bosonic sector. These tests will provide complementary information to other direct searches for new physics at the LHC. Many models predict deviations of vector boson self-couplings from the Standard Model at the $10^{-3} - 10^{-4}$ level [2]. Experiments that can reach this sensitivity could provide powerful constraints on these models. The signature for such anomalous couplings is enhanced diboson production cross sections, particularly at high transverse momentum ($p_T$) of the bosons. Experimental limits on non-Standard Model TGC's can be obtained by comparing the shape of the measured $p_T$ or mass distributions (or transverse mass, $M_T$, for final states involving $W$) with predictions, provided that the signal is not overwhelmed by background.

This work offers two improvements over previous ATLAS diboson studies [3]- [8]: First, the detector layout and the trigger system reflect the ATLAS experiment as it will operate at LHC turn-on. The analysis uses over 30 million fully simulated and reconstructed events, thus providing a more realistic understanding of the detection of these diboson final states. Second, a *Boosted Decision Trees* [9] technique is applied to selected channels, significantly enhancing measurement sensitivities.

## 1.1 Diboson production cross sections

Tree-level Feynman diagrams for electroweak diboson production at hadron colliders are shown in Figure 1. The *s*-channel diagram contains the vector-boson self-interaction vertices of interest here. The cross sections are calculated to next-to-leading-order (NLO) in [10]- [12]. The Standard Model diboson production cross sections are listed in Table 1.

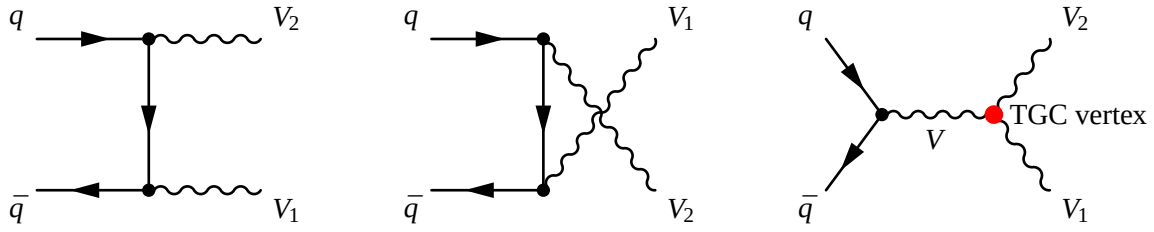


Figure 1: The generic Standard Model tree-level Feynman diagrams for diboson production at hadron colliders; $V, V_1, V_2 = \{W, Z, \gamma\}$. The *s*-channel diagram contains the trilinear gauge boson vertex.

The LHC diboson production rates will exceed those of the Tevatron by at least a factor 100 ($10\times$ higher in cross sections and at least $10\times$ higher in luminosity). Furthermore, because the energy reach at the LHC will be 7 times higher than at the Tevatron, the LHC sensitivity to anomalous TGC's is expected to be improved by orders of magnitude over those which can be reached at the Tevatron and LEP.

Table 1: The Standard Model diboson production total cross sections, calculated to the NLO, at the Tevatron ($\sqrt{s} = 1.96$ TeV) and the LHC ($\sqrt{s} = 14$ TeV). The references in the first column indicate the MC generators used for the calculations, with parton density function (PDF) CTEQ6M [13]. The theoretical uncertainly from PDF and scale factor is typically 5%.

| Diboson mode | Conditions | $\sqrt{s} = 1.96$ TeV $\sigma[pb]$ | $\sqrt{s} = 14$ TeV $\sigma[pb]$ |
|---|---|---|---|
| $W^+W^-$ [14] | $W$-boson width included | 12.4 | 111.6 |
| $W^\pm Z^0$ [14] | $Z$ and $W$ on mass shell | 3.7 | 47.8 |
| $Z^0Z^0$ [14] | $Z$'s on mass shell | 1.43 | 14.8 |
| $W^\pm\gamma$ [15] | $E_T^\gamma > 7$ GeV, $\Delta R(\ell,\gamma) > 0.7$ | 19.3 | 451 |
| $Z^0\gamma$ [16] | $E_T^\gamma > 7$ GeV, $\Delta R(\ell,\gamma) > 0.7$ | 4.74 | 219 |

### 1.2 Effective Lagrangian for charged TGC's

The most general effective Lagrangian, that conserves $C$ and $P$ separately, for charged triple gauge boson interactions is [17]:

$$L/g_{WWV} = ig_1^V(W^*_{\mu\nu}W^\mu V^\nu - W_{\mu\nu}W^{*\mu}V^\nu) + i\kappa^V W^*_\mu W_\nu V^{\mu\nu} + \frac{\lambda^V}{M_W^2}W^*_{\rho\mu}W^\mu_\nu V^{\nu\rho}$$

where $V$ refers to the neutral vector-bosons, $Z$ or $\gamma$, $X_{\mu\nu} \equiv \partial_\mu X_\nu - \partial_\nu X_\mu$ and the overall coupling constants $g_{WWV}$ are given by $g_{WW\gamma} = -e$, $g_{WWZ} = -e\,cot\theta_W$, with $e$ the positive electron charge and $\theta_W$ the weak mixing angle. The Standard Model triple gauge boson vertices are recovered by letting $g_1^V = \kappa^V = 1$ and $\lambda^V = 0$. Experimentally, deviations from the Standard Model couplings is searched for; thus the anomalous coupling parameters are defined as

$$\Delta g_1^Z \equiv g_1^Z - 1, \quad \Delta\kappa_\gamma \equiv \kappa_\gamma - 1, \quad \Delta\kappa_Z \equiv \kappa_Z - 1, \quad \lambda_\gamma, \quad \text{and} \quad \lambda_Z.$$

Note that electromagnetic gauge invariance requires $g_1^\gamma = 1$ or $\Delta g_1^\gamma = 0$.

Studies of three different diboson final states, $W^+W^-$, $W^\pm Z$ and $W^\pm\gamma$ will provide complementary sensitivities to the charged anomalous TGC's [16]. For example, the $\Delta\kappa_V$ terms in $W^+W^-$ production are proportional to $\hat{s}$, whereas these terms are only proportional to $\sqrt{\hat{s}}$ in $W^\pm Z$ and $W^\pm\gamma$ production. $W^+W^-$ production is thus expected to be more sensitive to $\Delta\kappa_V$ than $W^\pm Z$ and $W^\pm\gamma$ production. Conversely, $W^\pm Z$ production is expected to be more sensitive to $\Delta g_1^Z$ than $W^+W^-$ production because terms in $\Delta g_1^Z$ are proportional to $\hat{s}$ in $W^\pm Z$ production. The $\lambda$-type anomalous couplings have a strong $\hat{s}$ dependence in all three cases, thus the sensitivities will be enhanced at the high center-of-mass energy of the LHC.

### 1.3 Effective Lagrangian for neutral TGC's

In the Standard Model, neutral boson pairs, $ZZ$ and $Z\gamma$, are produced via the $t$-channel diagrams shown in Figure 1. While the Standard Model $ZZZ$ and $ZZ\gamma$ triple gauge boson couplings are zero at tree level, anomalous couplings may contribute. This study considers the effect of anomalous couplings on the production of pairs of on-shell $Z$ bosons only. In this case, the most general form of the $Z^\alpha(q_1)Z^\beta(q_2)V^\mu(P)$ ($V = Z,\ \gamma$) vertex function which respects Lorentz invariance and electromagnetic gauge invariance may be written as [18]

$$g_{ZZV}\Gamma^{\alpha\beta\mu}_{ZZV} = e\frac{P^2 - M_V^2}{M_Z^2}[\, if_4^V(P^\alpha g^{\mu\beta} + P^\beta g^{\mu\alpha}) + if_5^V\varepsilon^{\mu\alpha\beta\rho}(q_1 - q_2)_\rho\,]$$

where $M_Z$ is the Z-boson mass and $e$ is the positive electron charge; $q_1, q_2$ and $P$ are the 4-momenta of the two on-shell Z bosons and the $s$-channel propagator, respectively. The effective Lagrangian generating the $g_{ZZV}$ vertex function is

$$L = -\frac{e}{M_Z^2}[f_4^V(\partial_\mu V^{\mu\beta})Z_\alpha(\partial^\alpha Z_\beta) + f_5^V(\partial^\sigma V_{\sigma\mu})\tilde{Z}^{\mu\beta}Z_\beta],$$

where $V_{\mu\nu} = \partial_\mu V_\nu - \partial_\nu V_\mu$ and $\tilde{Z}^{\mu\beta} = \frac{1}{2}\varepsilon_{\mu\nu\rho\sigma}Z^{\rho\sigma}$. The couplings $f_i^V$ $(i = 4,\ 5)$ are dimensionless complex functions of $q_1^2,\ q_2^2$ and $P^2$ and are zero at tree level. All couplings are $C$ odd; $CP$ invariance forbids $f_4^V$, while parity conservation requires that $f_5^V$ vanishes. Because $f_4^Z$ and $f_4^\gamma$ are $CP$-odd, contributions to the helicity amplitudes proportional to these couplings will not interfere with the Standard Model terms, and hence $ZZ$ production is not sensitive to the sign of these couplings. The $CP$ conserving couplings $f_5^V$ contribute to the Standard Model cross section at the one-loop level, but this contribution is $\mathcal{O}(10^{-4})$ [18].

### 1.4 Current Tevatron results on diboson physics

Diboson production measurements and studies of anomalous TGC's have been performed at the Tevatron with the CDF and D0 experiments, using up to 2 $fb^{-1}$ of integrated $p\bar{p}$ luminosity. Diboson cross section measurements using $e/\mu$ decay modes, and their event statistics, measurement precision, and background events are summarized in Table 2. The measurments from Tevatron experiments [19]- [27] are consistent with the Standard Model predictions based upon NLO matrix element calculations.

Table 2: Summary of Tevatron $p\bar{p} \to$ diboson production cross sections

| Process | Source | L $\text{fb}^{-1}$ | observed events | background events | $\sigma$(data) [pb] $\pm$ (stat)$\pm$(sys)$\pm$(lum) | $\sigma$(theory) [pb] |
|---|---|---|---|---|---|---|
| $W^+W^-$ | CDF [19] | 0.83 | 95 | 38$\pm$5 | 13.6$\pm$2.3$\pm$1.6 $\pm$ 1.2 | 12.4$\pm$0.8 |
| ($ee$, $\mu\mu$, $e\mu$) | D0 [20] | 0.25 | 25 | 8.1$\pm$.5 | 13.8$\pm$4.1$\pm$1.1 $\pm$ 0.9 | ” |
| $W^\pm Z$ | CDF [21] | 1.1 | 16 | 2.7$\pm$0.4 | $5.0^{+1.8}_{-1.4} \pm 0.4$ | 3.7$\pm$0.3 |
| ($\ell^\pm\nu\ell^+\ell^-$) | D0 [22] | 1.0 | 13 | 4.5$\pm$0.6 | 2.7 +1.7$-$1.3 (total) | ” |
| $Z\gamma$ | CDF [23] | 0.2 | 72 | 4.9$\pm$1.1 | 4.6 $\pm$0.6 (sta+sys) $\pm$ 0.3 | 4.5$\pm$0.3 |
| ($\ell^+\ell^-\gamma$) | D0 [24] | 1.0 | 968 | 117$\pm$12 | 4.96 $\pm$0.3 (sta+sys) $\pm$ 0.3 | 4.7$\pm$0.2 |
| $W^\pm\gamma$ | CDF [23] | 0.2 | 323 | 114$\pm$21 | 18.1 $\pm$3.1 (sta+sys) $\pm$ 1.2 | 19.3$\pm$1.4 |
| ($\ell^\pm\nu\gamma$) | D0 [25] | 0.16 | 273 | 132$\pm$7 | 14.8 $\pm$1.9 (sta+sys) $\pm$ 1.0 | 16.0$\pm$0.4 |
| $ZZ$ | CDF [26] | 1.9 | 2 | 0.014 | $1.4^{+0.7}_{-0.6}\pm 0.6$ | 1.5$\pm$0.2 |
| ($\ell^+\ell^-\ell^+\ell^-$) | D0 [27] | 1.0 | 1 | 0.13 | $< 4.4$ | ” |

The Tevatron's $p\bar{p}$ collisions produce the charged states of $W^\pm Z$ and $W^\pm\gamma$. These states can be used to study the $W^+W^-Z$ and the $W^+W^-\gamma$ couplings independently, which is in contrast with the anomalous TGC measurements made at LEP [30] from the $W^+W^-$ final state, where certain assumptions relating the $W^+W^-Z$ and the $W^+W^-\gamma$ couplings were made. The Tevatron limits for the $WW\gamma$ and WWZ TGC's are summarized in Table 3 [25]- [22]. These limits will improve significantly by combining the constraints from the $W^\pm\gamma$, $W^\pm Z$ and $W^+W^-$ channels, and by increasing the datasets using the expected integrated luminosity of 6 $\text{fb}^{-1}$ at the end of the Tevatron running.

Table 3: Anomalous gauge coupling limits (95% C.L.) for $WW\gamma$ and $WWZ$ from the Tevatron experiments.

| Coupling | Source | L ($fb^{-1}$) | $\lambda_Z$ | $\Delta\kappa_Z$ | $\Delta\kappa_\gamma$ | $\lambda_\gamma$ |
|---|---|---|---|---|---|---|
| $WW\gamma$ from $W^\pm\gamma$ | D0 [25] | 0.16 | | | [-0.88, 0.96] | [-0.2, 0.2] |
| $WWZ$ from $W^\pm Z$ | D0 [22] | 1.0 | [-0.17, 0.21] | [-0.12, 0.29] | | |
| $WWZ$ from $W^\pm Z$ | CDF | 1.9 | [-0.13, 0.14] | [-0.82, 1.27] | | |
| $WWZ = WW\gamma$ from $W^+W^-$ | D0 [28] | 0.25 | [-0.31, 0.33] | [-0.36, 0.33] | | |
| from $W^+W^-$, $W^\pm Z$ | CDF [29] | 0.35 | [-0.18, 0.17] | [-0.46, 0.39] | | |

# 2 Signal and background modeling and simulated data samples

## 2.1 MC generators used to produce fully simulated events

The diboson physics analyses focus on leptonic decay channels of the boson pairs ($W^+W^-$, $W^\pm Z$, $ZZ$, $W^\pm\gamma$, and $Z\gamma$) produced in the proton-proton collisions at the LHC.

On-shell diboson production of the $W^+W^-, W^\pm Z, ZZ$ final states, and subsequent pure leptonic decays, are modeled by the MC@NLO [14] Monte Carlo generator, which incorporates the next-to-leading-order (NLO) QCD matrix elements into the parton shower by interfacing to the HERWIG/Jimmy [31] programs. The gauge-boson decays into tau leptons are included in the MC event generator and these tau leptons decay to all the possible final states. Hard emission is treated as in NLO computations and soft/collinear emission is treated as in regular parton shower MC. The matching between these two regions is smooth (no double-counting). $W$-boson width and spin-spin correlations are included in the generator. However, 'zero-width' approximations are used in $W^\pm Z$ and $ZZ$ calculations, and no $Z/\gamma^*$ interference terms are included. MC@NLO does not include anomalous triple gauge boson couplings. The process of $W^+W^-$ production via gluon-gluon fusion and the leptonic decays of the $W$, $gg \to W^+W^- \to \ell\nu\ell'\nu$, is modeled by the MC generator `gg2ww` [32]. The $W^\pm\gamma$ and the $Z\gamma$ production processes and subsequent leptonic decays of the $W^\pm$ and the $Z$ are modeled by the PYTHIA MC generator [33], which only incorporates the leading-order (LO) QCD matrix elements into the parton shower. To include the off-shell $Z$ and $\gamma^*$ into the $ZZ$ analysis, we have also used PYTHIA to generate the $Z/\gamma^* + Z/\gamma^* \to \ell^+\ell^-\ell'^+\ell'^-$ events. The $Z/\gamma^*$ mass threshold is set to 12 GeV in PYTHIA. Table 4 list all the diboson signal samples used in this paper.

Major physics backgrounds for diboson signal detection come from top pairs and QCD jets associated with $W$ or $Z$ gauge bosons. We have used MC@NLO to model $t\bar{t} \to \ell + X$ production (700k events). The inclusive $W + X$ and $Z + X$ ($X$ = jets, or $\gamma$) processes are modeled by the PYTHIA (30M events) and ALPGEN [34] (1.1M events).

## 2.2 MC generators for TGC studies

Monte Carlo generators BHO [16] and BosoMC [15] are used for anomalous TGC studies. These MC programs are numerical parton level generators. They are used to calculate both LO and NLO cross sections for all five diboson final states ($W^+W^-$, $W^\pm Z$, $ZZ$, $W^\pm\gamma$, $Z\gamma$) with anomalous coupling parameters. However, they do not include parton showers automatically. We use the BHO MC to model the $ZZ$, $W^+W^-$, and $Z\gamma$ production cross sections and kinematics with Standard Model and anomalous couplings. BosoMC is used for $W^\pm Z$ and $W^\pm\gamma$ diboson final-state TGC studies. The calculated diboson production rates from these generators are accurate to NLO. The $W^+W^-$, $W^\pm Z$ and $ZZ$ production

Table 4: Diboson signal production processes, cross sections and fully simulated number of MC events. The MC simulation 'filter' is the event selection at the generator level. The corresponding filter efficiencies are given in the table. We also indicate the MC generators used to produce the MC events and to calculate the cross sections given in this table.

| Process | cross section (fb) | $\varepsilon_{\text{filter}}$ | $N_{MC}$ | Generator |
|---|---|---|---|---|
| $q\bar{q}' \to W^+W^- \to \ell^+\nu\ell^-\nu$ | 11718 | 1.0 | 180,000 | MC@NLO |
| $gg \to W^+W^- \to \ell^+\nu\ell^-\nu$ | 540.0 | 0.96 | 180,000 | `gg2ww` |
| ($\ell = e,\ \mu,\ \tau$) | | | | |
| $q\bar{q}' \to W^+Z^0 \to \ell^+\nu\ell^+\ell^-$ | 441.7 | 1.0 | 50,000 | MC@NLO |
| $q\bar{q}' \to W^-Z^0 \to \ell^-\nu\ell^+\ell^-$ | 276.4 | 1.0 | 50,000 | MC@NLO |
| ($\ell = e,\ \mu$; $Z^0$ on mass shell) | | | | |
| $q\bar{q}' \to Z^0Z^0 \to \ell^+\ell^-\ell^+\ell^-$ | 66.8 | 1.0 | 49,250 | MC@NLO |
| $q\bar{q}' \to Z^0Z^0 \to \ell^+\ell^-\nu\bar{\nu}$ | 397 | 1.0 | 118,000 | MC@NLO |
| ($\ell = e,\ \mu$; $Z^0$ on mass shell) | | | | |
| $q\bar{q}' \to Z^0Z^0 \to \ell^+\ell^-\ell^+\ell^-$ | 159 | 0.219 | 43,000 | PYTHIA |
| ($\ell = e,\ \mu,\ \tau$; $M_{Z^0/\gamma^*} > 12$ GeV ) | | | | |
| (4 leptons ($e,\ \mu$), $p_T^\ell > 5$ GeV, $\lvert\eta^\ell\rvert < 2.7$) | | | | |
| $q\bar{q}' \to W^+\gamma \to \ell^+\nu\gamma$ | 10220 | 1.0 | 38,400 | PYTHIA |
| $q\bar{q}' \to W^-\gamma \to \ell^-\nu\gamma$ | 6820 | 1.0 | 25,600 | PYTHIA |
| ($\ell = e,\ \mu$; $E_T^\gamma > 10$ GeV ) | | | | |
| $q\bar{q}' \to Z^0\gamma \to \ell^+\ell^-\gamma$ | 5280 | 1.0 | 66,000 | PYTHIA |
| ($\ell = e,\ \mu$; $E_T^\gamma > 10$ GeV ) | | | | |

calculations with the Standard Model couplings are compared with the MC@NLO calculations using PDF CTEQ6M. We found that both cross sections and kinematic distributions are in good agreement, as shown in Figure 2. The left plot shows the $W^\pm Z$ production differential cross section as a function of the transverse mass of the $W^\pm Z$ system. The right plot shows the $W^+W^-$ production differential cross section as a function of the $W$ transverse momentum. The discrepancies between MC@NLO and the BHO MC are within 2%.

A somewhat different procedure is used in the estimation of neutral triple gauge couplings from ZZ events. In this case, the signal expectation with anomalous couplings was determined from the leading order Monte Carlo calculation of BHO [16], corrected using a $p_T$ dependent k-factor derived from MC@NLO.

# 3 Diboson event selection

This section discusses features of five diboson signals, ($W^\pm Z$, $W^\pm\gamma$, $W^+W^-$, $Z\gamma$, $ZZ$), the major backgrounds and the analysis cuts required to discriminate between them. The varied event topolology of each diboson signal precludes a common set of universal cuts. Two analysis approaches are employed. The first is based on a sequence of straight cuts on kinematic quantities. The second is a refined, multivariate analysis based on Boosted-Decision-Trees (BDT) which is briefly described in the following section. Some of the diboson analyses employ both techniques. The major results of these analyses are included here.

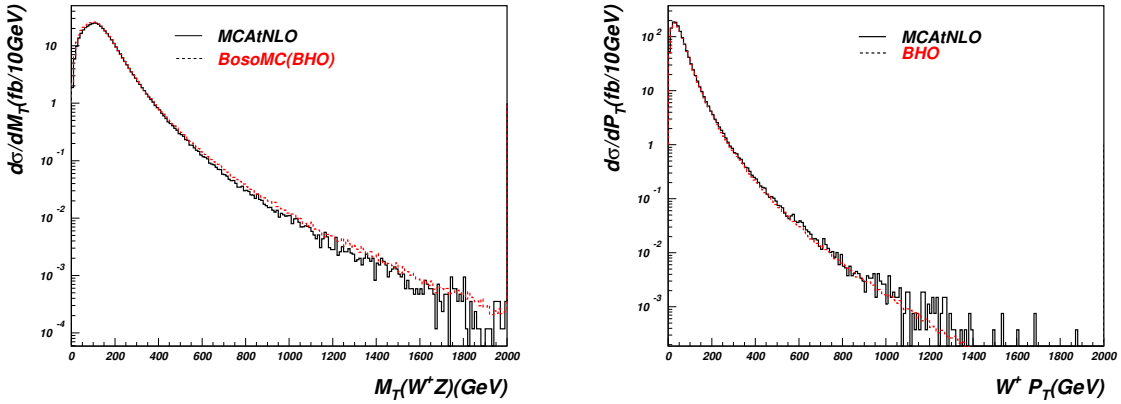


Figure 2: Comparison of MC@NLO MC to BHO MC for $W^{\pm}Z$ and $W^{+}W^{-}$ production. The histograms are normalized to production cross sections. Left plots: the $W^{\pm}Z$ $M_T$ distributions from $W^{\pm}Z$ production. Right plots: the W $p_T$ distributions from $W^{+}W^{-}$ production.

### 3.1 Physics objects

The ATLAS detector and its performance is described in detail elsewhere [35]. A brief description of the physics objects used in diboson analysis is given below.

The major physics objects used in diboson physics analysis are electrons, photons, muons, missing $E_T$ ($\not\!\!E_T$), and hadronic jets. Electrons are identified by their distinctive pattern of energy deposition in the calorimeter and by the presence of a track in the inner tracker that can be extrapolated from the interaction vertex to a cluster of energy in the calorimeter. To ensure high trigger efficiency, for events with a single electron, the transverse energy of an single electron must satisfy $E_T > 25$ GeV. For events with di-electrons, both electrons are required to have $E_T > 10$ GeV. The electrons must be isolated from other energy clusters. An electron is required to pass a set of cuts on shower shape, track quality and track to calorimeter cluster matching. Photon identification is similar to an electron in the EM calorimeter, but no charged tracks in the inner tracker should match the EM energy cluster. The average electron identification efficiency in the barrel is about 75% and in the endcaps about 60%.

Muons are reconstructed using information from the outer muon spectrometer (MDT chambers and trigger chambers), the inner tracking detectors and the calorimeters. Muons are identified with a tracking algorithm that associates a track found in the muon spectrometer with the corresponding inner detector track, after the former is corrected for energy loss in the calorimeter. The combined muon detection rapidity coverage is $|\eta| < 2.5$. The minimum $p_T$ of reconstructed muon track is 5 GeV. The candidate muons are required to be isolated in the calorimeter and inner tracker to minimize the contributions of muons originating from QCD jets. The average muon identification efficiency is about 95%.

The hadronic jets are reconstructed using the fixed-cone jet algorithm. The cone size used in this analysis is 0.7. The jet seed threshold on the transverse energy in a tower is set to $E_s = 1$ GeV, and the final energy cut on a jet is $E_T > 7$ GeV. With this cut the minimum measurable jet $E_T$ should be 20GeV.

Missing transverse energy, $\not\!\!E_T$, is calculated from the energy deposited in all calorimeter cells and from muons. A correction is applied for the energy lost in the cryostat. For diboson events with neutrinos in final states, the $\not\!\!E_T$ resolution is about 6.5GeV.

The ATLAS trigger consists of three levels of event selection: Level-1 (L1), Level-2 (L2) and the event filter (EF). The L2 and EF together form the High-Level Trigger (HLT). According to the present physics trigger menu for initial running, diboson candidate events with multi-lepton final states will be recorded with single muon, single electron, di-electron and di-muon triggers. The trigger efficiencies for diboson events, defined as the fraction of events accepted by the analysis cuts that have satisfied

the trigger requirements, are expected to be in a range of 95% - 100%, with the exception of a lower efficiency ($\sim$ 90%) for $W\gamma$ events.

### 3.2 Boosted decision trees

A rather new multivariate analysis technique, *Boosted-Decision-Trees* (BDTs), has been used in our analysis to improve the detection sensitivity for diboson signals. BDTs have been used in HEP data analysis in recent years [36], and details can be found in the reference [9]. A further development, allowing for weighted events, is used in these diboson physics studies [37].

The BDT technique involves a 'training' procedure for event pattern recognition. It works with a set of data including both *signal* and *background*. Data are represented by a set of physics variable distributions. A *decision-tree* splits data recursively based on *cuts* on the input variables until a stopping criterion is reached. Every event ends up in a *signal* (score=1) or a *background* (score=-1) *leaf* of the decision-tree. Misclassified events will be given larger weights in the next tree (boosting). This procedure is repeated several hundreds to thousands of times until the performance is optimal. The *discriminator* from the BDT training is the sum of the weighted scores from all the decision-trees. If the total score for a given event is relatively high this event is most likely a signal event, and if the score is low it is likely a background event.

### 3.3 $W^{\pm}Z \to \ell^{\pm}\nu\ell^{+}\ell^{-}$ selection

The $W^{\pm}Z$ production at hadron colliders is mainly the result of the $WWZ$ trilinear gauge boson couplings as shown in Figure 1, the SM tree-level Feynman diagrams.

$W^{\pm}Z$ candidate events have three charged lepton final states, referred to as trileptons, produced when $Z \to \ell^{+}\ell^{-}$ and $W^{\pm} \to \ell^{\pm}\nu$, where $\ell^{\pm}$ are $e^{\pm}$ or $\mu^{\pm}$. SM backgrounds can be highly suppressed by requiring three isolated high $p_T$ leptons and large missing transverse energies ($\not\!\!E_T$). However, the pure leptonic decay mode of the $W^{\pm}Z$ events only has a 1.5% branching ratio [38]. The total cross sections times the branching ratio are 441.7 fb and 276.4 fb for $W^{+}Z$ and $W^{-}Z$, respectively. Event selection with high efficiency is important for early observations of this channel.

Major backgrounds to the $W^{\pm}Z$ trilepton final states come from $ZZ \to \ell^{+}\ell^{-}\ell^{+}\ell^{-}$ with one lepton undetected; $Z + X \to \ell^{+}\ell^{-} + X$ (X=jets, or photon) with a jet or a photon faking a lepton; and $t\bar{t} \to W^{+}W^{-}b\bar{b} \to \ell + \ell + \ell + X$.

After a trigger, $W^{\pm}Z$ events are selected in two stages: (1) pre-selection with relatively loose cuts, and (2) final selection with tightened cuts or with BDT multivariate discriminator. The overall trigger efficiency for $W^{\pm}Z$ events with trileptons in the final state is (98.9$\pm$ 1)% using a combination of single lepton and dilepton triggers.

The pre-selection of the $W^{\pm}Z$ events is done by identifying three leptons (at least one lepton with $p_T > 25$ GeV) and requiring $\not\!\!E_T > 15$ GeV in an event with characteristics consistent with $Z$ dilepton decays ($M_{\ell\ell} = (91.18 \pm 20)$ GeV) and $W$ leptonic decays (10 GeV $< M_T(\ell, \not\!\!E_T) <$ 400 GeV). The overall pre-selection efficiency for $W^{+}Z$ events is 25.8%, and for $W^{-}Z$ events is 29.3%. The acceptance difference is due to the differing $\eta$ distributions of the leptons decaying from $W^{+}$ and $W^{-}$. After the preselection, the known background is about 70 times larger than the signal size.

To bring the background level below the signal, a rejection power better than 100 in the second stage of event selections is required. To achieve this, events with $\not\!\!E_T < 25$ GeV and with significant hadronic jet activities are rejected. Events must contain no more than one hadronic jet with $E_T^{jet} > 30$ GeV and $|\eta^{jet}| < 3.0$. The transverse recoil of the $W^{\pm}Z$ system, calculated using the vector sum of the $p_T$ of the charged leptons and $\not\!\!E_T$, is required to be less than 120 GeV and the sum of the hadronic transverse energy must be less than 200 GeV. These requirements effectively reject the $t\bar{t}$ and QCD jet events. To reject the $Z + X$ background, the lepton $p_T$ is required to be greater than 20 GeV and 25 GeV for muons

Table 5: Number of expected $W^{\pm}Z$ signal ($N_{WZ}$) and background ($N_B$) for 1 fb$^{-1}$ data with cut-based analysis.

| | $WZ$ | $ZZ$ | $t\bar{t}$ | $Z+$jet | $Z+\gamma$ | DY | Total bkg | $N_{WZ}/N_B$ |
|---|---|---|---|---|---|---|---|---|
| $N$ events | **53.43** | 2.68 | 0.023 | 1.89 | 0.18 | 2.52 | **7.30** | 7.32 |
| % of background | - | 36.71 | 0.32 | 25.92 | 2.47 | 34.58 | - | - |

Table 6: Number of expected $W^{\pm}Z$ signal (with BDT selection efficiency after pre-selection), and background ($N_B$) for 1 fb$^{-1}$ of data with BDT analysis using the cut BDT $> 200$.

| | $WZ$ | $ZZ$ | $t\bar{t}$ | $Z+$jet | $Z+\gamma$ | Other | Total bkg | $N_{WZ}/N_B$ |
|---|---|---|---|---|---|---|---|---|
| $N$ events | **152.6 (65%)** | 7.7 | 2.8 | 2.5 | 2.0 | 1.1 | **16.1** | 9.5 |
| % of background | | 47.8 | 17.4 | 15.5 | 12.5 | 7.0 | - | - |

and electrons, respectively. Any pair of leptons must satisfy $\Delta R = \sqrt{(\Delta\eta^2 + \Delta\phi^2)} > 0.2$. Leptons must be isolated from other energy clusters based on calorimeter and inner tracker measurements. All three leptons must be associated with isolated tracks that originate from the same collision point. The dilepton invariant mass best matching the mass of $Z$ must be within the $Z$-mass window of $|M_Z - M_{\mu\mu}| < 12$ GeV or $|M_Z - M_{ee}| < 9$ GeV. These mass windows are set by the mass resolution. The $M_T$ determined by the third lepton (not from $Z$ decay) and the $\not{E}_T$ must be within the transverse $W$-mass window: 40 GeV $< M_T < 120$ GeV.

The total and selected number of the signal and the background events for each trilepton final state, and for 1 fb$^{-1}$ of integrated luminosity, are listed in Table 5. The overall signal efficiency is 8.7% and 7.1% for $W^-Z$ and $W^+Z$, respectively. For 1 fb$^{-1}$ of data, 53 $W^{\pm}Z$ signal events and 8 background events are expected. The dominant background contributions are from $ZZ$, $Z$+Jet and Drell-Yan (DY) processes, while $Z\gamma$ and $t\bar{t}$ contribute a small fraction of the total background events.

For 0.1 fb$^{-1}$ of integrated luminosity, only 5 signal events with 1 background event contamination are expected. The $W^{\pm}Z$ detection significance will be only $4\sigma$. To improve the detection sensitivity the Boosted-Decision-Trees analysis technique is employed. This BDT analysis is conducted for a total 1000 trees with 20 tree-split nodes. Based on the variables used in the cut-based analysis, and the BDT training Gini-index (a measure of a variable effectivness in separating signal from background), a total of 22 kinematic and topology variables are selected for the BDT training. About 12000 pre-selected signal events and 18000 pre-selected background events are used in this BDT-based analysis, where 50% of the signal and background events are used for the **training**, and another 50% of statistically independent events allocated to the BDT **test** sample sets. The BDT output discriminator from the testing sample, used to separate the signals from the background, is shown in Figure 8 (right), see Section 4. This spectrum will be used to determine (fit) the $W^{\pm}Z$ production cross section.

Results of the $W^{\pm}Z$ event selection with the cut BDT $> 200$ are shown in Table 6. Expected numbers of signal and background events are given for 1 fb$^{-1}$ of integrated luminosity. The estimated background uncertainties are 15-20% due to the limited number of simulated events available. The overall $W^{\pm}Z$ event selection efficiency is about 18% for a signal to background ratio close to 10. Using the BDT analysis, the $W^{\pm}Z$ detection sensitivity in terms of Poisson statistical significance should exceed 7 for the first 0.1 fb$^{-1}$ of integrated luminosity.

### 3.4 $W^{\pm}\gamma \to \ell^{\pm}\nu\gamma$ selection

The production of the charged diboson final state $W^{\pm}\gamma$ is sensitive to the triple gauge boson $WW\gamma$ coupling in the $s-$channel as shown in Figure 1. The $W^{\pm}\gamma$ diboson events are selected from the $pp$ collisions using pure $W$ leptonic decays. The $W^{\pm}\gamma$ signal events are modeled with PYTHIA, which includes tree-level diagrams for $W$ production with initial state radiation (ISR) and $s-$channel production depending on the triple-gauge-coupling $WW\gamma$ vertex. The $WW\gamma$ vertex introduces a destructive interference of *zero amplitude* at $\cos\theta^{-}_{\bar{q},\gamma} = \pm 1/3$ for $W^{\pm}$ production, where $\theta^{-}_{\bar{q},\gamma}$ is the photon scattering angle to the incoming anti-quarks.

The experimental signature is a final states with one high $p_T$ lepton (electron or muon), one high $p_T$ photon and large $\not\!\!E_T$. Major backgrounds are from the processes:

- Inclusive $W+X$ production with $W+X \to \ell\nu+X$ , where the $\gamma$ is from final state radiation (FSR) from the lepton.
- Inclusive $W+X \to \ell\nu+X$ productions, with $X = jets$ and the jets faking a photon.
- Inclusive $Z+X \to \ell\ell+X$ productions, with one lepton escaping detection, and with $X = \gamma$ or jets faking a photon.

A photon isolation cut is effective in suppressing these backgrounds.

To study the $W^{\pm}\gamma$ detection sensitivity about 1.3 million inclusive $W$ events and about 100,000 inclusive $Z$ events were generated with the PYTHIA MC generator. In these datasets, the photon transverse energy threshold is 10 GeV and the lepton and photon separation, $\Delta R(\ell,\gamma)$ was required to be greater than 0.7.

The $W^{\pm}\gamma$ candidates are inclusive $e^{\pm}\gamma$ or $\mu^{\pm}\gamma$ events having one electron or muon observed and the absence of the oppositely charged lepton of the same flavor. The photon selected is the most energetic one in the events. Efficiencies for three trigger types are investigated: isolate muon with $p_T > 20$ GeV, isolate electron with $p_T > 25$ GeV and photon with $E_T(\gamma) > 60$ GeV. The overall $W^{\pm}\gamma$ trigger efficiency is about 90%.

Background to the $W^{\pm}\gamma$ signal is dominated by inclusive $W^{\pm}$ events with radiated jets faking a photon. Contamination from inclusive $Z$ events with an undetected lepton is also significant. Figure 3 shows $W^{\pm}\gamma$ signal (first column) scattering plots comparing with major backgrounds: the inclusive $W$ events with final state radiation (FSR) (the 2nd column), and with fake photon (the third column), and the $Z$ events with one lepton escaping detection and a photon of any type reconstructed (the 4th column).

Table 7: The number of $W^{\pm}\gamma$ signal and background events after pre-selection and BDT selection, for an integrated luminosity of 1fb$^{-1}$. The signal and total background are then scaled to NLO cross sections with the the k-factors indicated.

| | | Signal | Background | | | |
|---|---|---|---|---|---|---|
| | | $W^{\pm}\gamma$ | W+FSR_$\gamma$ | W+fake_$\gamma$ | $Z(\ell\ell)\gamma$ | Total |
| $\ell = e$ | Pre-selected | 1762 | 7890 | 32480 | 1710 | |
| | BDT selection | 1145 | 242 | 791 | 101 | |
| | NLO scaled | 1901 (k=1.66) | | | | 1474 (k=1.3) |
| $\ell = \mu$ | Pre-selected | 2758 | 10250 | 3950 | 2680 | |
| | BDT selection | 1793 | 413 | 961 | 409 | |
| | NLO scaled | 2976 (k=1.66) | | | | 2318 (k=1.3) |

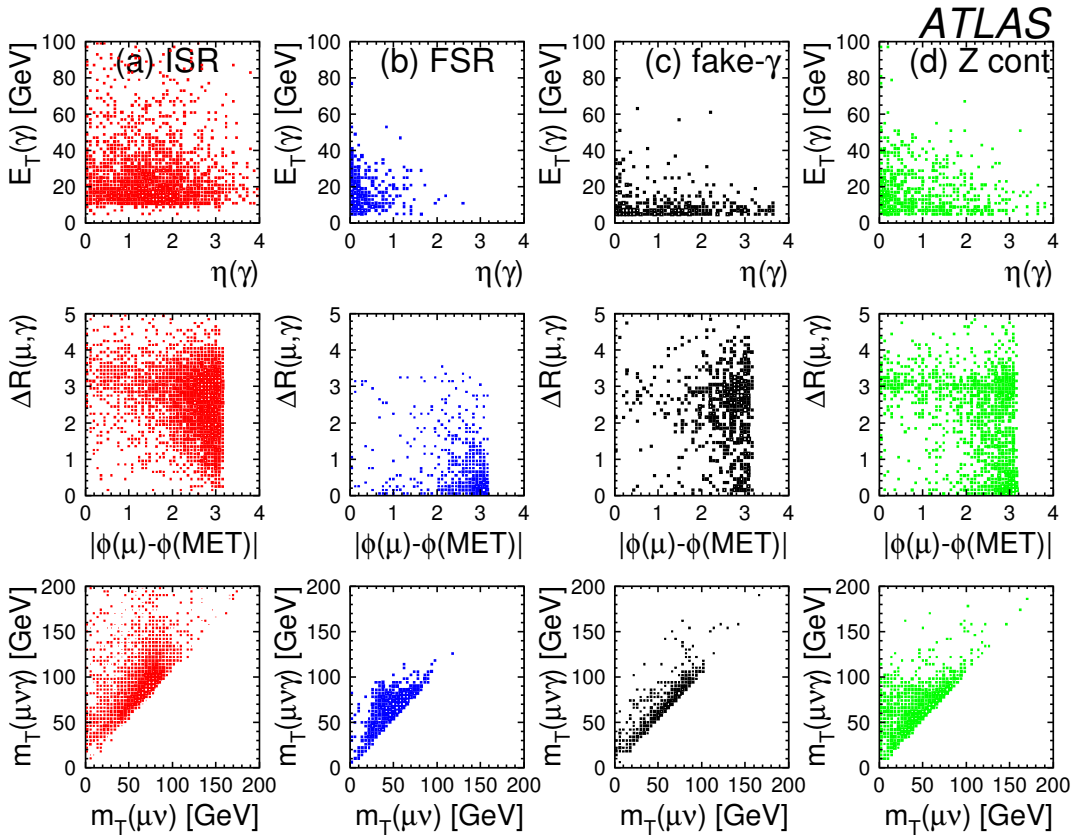


Figure 3: Distributions of the $W^{\pm}(\mu^{\pm}\nu)\gamma$ event variables, with a photon from ISR, FSR, and fake backgrounds, and inclusive $Z$ contamination.

The Boosted Decision Tree method is used to select the $W^{\pm}\gamma$ events. Three trainings are done to separate: 1) FSR photons from other sources, 2) signal photons from fake photons, and 3) signal photons from the contamination of $Z$ inclusive events. Nineteen variables are used in the BDT analysis. Cuts are applied to the BDT output spectra for the three trainings. The cuts chosen for signal selection corresponds to a $W^{\pm}\gamma$ selection efficiency of 65% with a signal to background ratio of 0.95 (0.98) for electron (muon) final states, respectively. The numbers of events selected with the BDT cuts are listed in Table 7.

The BDT discriminates signal photons effectively from FSR and fake photons in the high $E_T(\gamma)$ region. This preserves a high detection efficiency in the region that is sensitive to discovery of phenomenon beyond Standard Model predictions.

### 3.5 $W^+W^- \to \ell^+\nu\ell^-\nu$ selection

The production of $W$ pairs has been investigated extensively at LEP and at Tevatron. The experimental $W^+W^-$ signature is two high transverse momentum leptons with opposite charge associated with large transverse missing energy. $W^+W^-$ production involves both $WWZ$ and $WW\gamma$ triple gauge boson couplings and is most sensitive to the $\Delta\kappa_V$ anomalous coupling parameters. Furthermore, the $W$ pair production provides an important background to Higgs boson searches in the $pp \to H \to W^*W^* \to \ell\nu\ell\nu$ channel at the LHC. In dileptonic $W$-decays no Higgs mass peak can be reconstructed, so this background cannot be estimated from the measured data via sideband interpolation. An understanding of the irreducible $W$-pair continuum background is therefore crucial.

Table 8: Yield of the WW selection for 1 fb$^{-1}$ of data. The errors shown are statistical only.

| | efficiency | | $N_{WW}$ | | $N_{\text{background}}$ | $N_{\text{sig.}}/N_{\text{bkg.}}$ |
|---|---|---|---|---|---|---|
| Selection-A | $gg \to WW$ | $q\bar{q} \to WW$ | $gg \to WW$ | $q\bar{q} \to WW$ | | |
| $ee$ | 2.1% | 1.33% | 1.25±0.05 | 17.4 ± 1.1 | 1.4 ±0.3 | 13.3±3.0 |
| $\mu\mu$ | 4.1% | 2.80% | 2.43±0.08 | 36.4 ± 2.2 | 10.7 ± 2.1 | 3.6± 0.8 |
| $e\mu$ | 2.8% | 1.94% | 3.33±0.13 | 50.6± 1.8 | 7.2 ± 1.2 | 7.5 ± 1.3 |
| $ll$ | 3.0% | 2.00% | 7.00±0.16 | 104.4±2.4 | 19.3±2.4 | 5.8 ± 0.8 |
| Selection-B | | | | | | |
| $ee$ | 0.94% | 0.92% | 0.6±0.04 | 12.0 ± 0.9 | 2.8± 1.2 | 4.5 ± 1.9 |
| $\mu\mu$ | 2.1% | 1.96% | 1.1±0.03 | 25.5 ± 1.8 | 4.8±1.0 | 5.5 ±1.2 |
| $e\mu$ | 1.3% | 1.36% | 1.54± 0.09 | 35.3 ± 1.5 | 7.4± 1.3 | 5.0 ± 0.9 |
| $ll$ | 1.4% | 1.40% | 3.24±0.10 | 72.8 ±2.5 | 15.0 ± 2.0 | 5.1 ± 0.8 |

At the LHC the major background processes ($t\bar{t}$, inclusive $W$ and $Z$, and Drell-Yan) have much higher cross sections than $W^+W^-$. It will be necessary to achieve very high background rejection power to suppress the events with mis-identified leptons (from jet, photon and instrumentation effects) and leptons decay from the heavy-flavor quark jets. In the DY process the mis-measured $\not{E}_T$ also contributes non-negligible background.

Event selection consists of the trigger, pre-selection (two high $p_T$ leptons plus $\not{E}_T$), and final selection with a set of conventional cuts or with BDT selection cuts. The $W^+W^-$ events are required to pass one of two high-level trigger paths: a single, isolated electron with $p_t > 25$ GeV or a single muon, with $p_t > 20$ GeV. The trigger efficiencies for $WW \to ee$, $WW \to \mu\mu$ and $WW \to e\mu$ events with two opposite sign isolated leptons ($p_T > 20$ GeV, $|\eta| < 2.5$) are given as follows: 98.2 %, 95.9%; and 97.4% respectively.

The cut based analysis rejects background events with tight lepton identification criteria and isolation requirements as well as with event topology variables which clearly distinguish the signal and significantly suppress the main background processes $t\bar{t}$ and $Z+X$. The $W^+W^-$ leptonic decay events are selected by requiring two well identified isolated leptons with opposite charge, and with $p_T^l > 20$ GeV and $|\eta| < 2.5$. A jet veto requirement rejects events with any jet ($p_T^{jets} > 20$ GeV) in the rapidity region $|\eta| < 3$. This cut is efficient in $t\bar{t}$ suppression since $t\bar{t}$ contains one or two energetic $b$ jets in addition to the $W^+W^-$ signature. An event with $\not{E}_T < 50$ *GeV* is rejected to reduce the background arising from the event pileup and from $Z/\gamma*$ events in the DY process. To reject the dilepton events from inclusive $Z$ production, a $Z$ mass veto is applied. Finally, angular variable cuts are imposed. For cross section measurements, events must pass a cut: $\phi_{\ell\ell} < 2$ rad, where $\phi_{\ell\ell}$ is the angle between the transverse momentum of the two leptons. For anomalous TGC studies, this cut is replaced with: $\Phi(\mathbf{p}_T^{\ell^+,\ell^-}, \mathbf{p}_T^{miss}) > 175^0$, where $\Phi$ is the angle between the transverse momenta of the lepton pair, and the missing transverse momentum. The first angular cut (selection-A) results in high signal detection efficiency, but it is not optimized for high $p_T(\ell)$ and $p_T(\ell\ell)$ event detection and thus could decrease the sensitivity to anomalous TGC's. The second angular cut (selection-B) results in lower signal detection efficiencies, but has higher efficiency for high $p_T(\ell)$ and $p_T(\ell\ell)$ events. The yields of the $W^+W^-$ selection with cut-based analysis are summarized in Table 8. Both signal and background events are normalized to 1 fb$^{-1}$ of data. Figure 4 shows the transverse momentum distributions of leptons (left) and lepton pairs (right) after applying kinematic cuts of Selection-B. The distributions are shown for sum of signal and various backgrounds, and for individual backgrounds, for an integrated luminosity of 1fb$^{-1}$ of data.

With the cut based event selection, the $W^+W^-$ overall signal detection efficiency is 1.4-2%. The

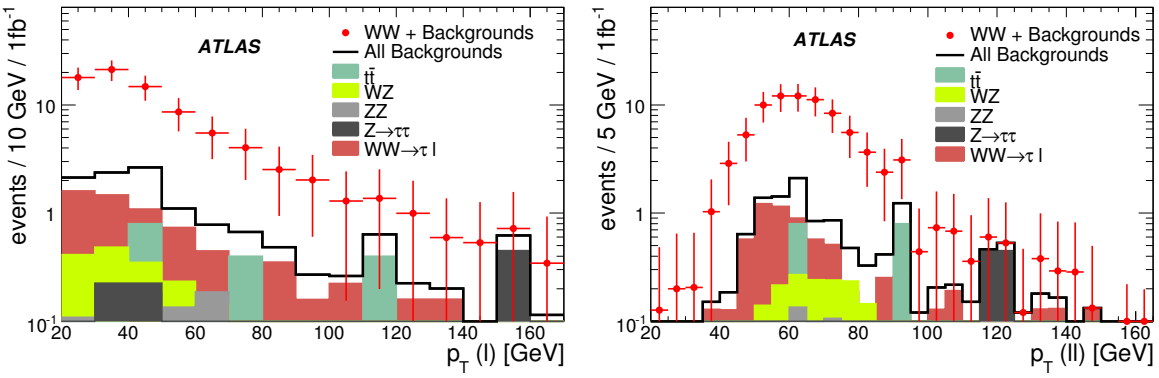


Figure 4: Transverse momentum distributions of leptons (left) and lepton pairs (right) after applying kinematic cuts from Selection-B. The distributions are shown for sum of signal and various backgrounds, and for separated backgrounds for L=1 fb$^{-1}$.

signal detection significance for 0.1 fb$^{-1}$ of data is expected to be below $5\sigma$ (for selection-B). The detection efficiencies can be improved by using the multivariate BDT technique. In this $W^+W^-$ analysis one thousand decision trees, wherein one tree has 20 $splitting-nodes$, are used to separate signal from background based on the input variables. The input data for the BDT analysis must first pass the pre-selection cuts (two leptons with $p_T^\ell > 10$ GeV and $\not{E}_T > 15$ GeV. The pre-selected simulated samples are divided into two equal parts: one sample is used for BDT training and the other to test event selection performance. The BDT output spectra for both signal and background are shown in Figure 8 (left). By varying the location of the cut along the BDT *scores* (x-axis), the signal to background ratio can be optimized. Table 9 presents the detection sensitivities with total integrated luminosity of 1 fb$^{-1}$; the selected number of signal events ($N_{WW}$), the corresponding signal efficiency (Eff$_{WW}$), the number of background ($N_{bkg.}$) events, and signal to background ratio ($N_{WW}/N_{bkg}$) are shown. For initial measurements using early LHC data based on only 0.1 fb$^{-1}$ of integrated luminosity, application of BDT is compelling. As inferred from Table 8, this initial data are expected to yield a total for all decay channels of $\sim 8$ signal events using conventional cuts, whereas the BDT-based analysis, which gives the same signal to background ratio of 5 as the conventional cuts, produces an expectation of $\sim 57$ signal events.

Table 9: $WW \rightarrow$ leptons detection sensitivities of accepted signal and background events for 1 fb$^{-1}$ of integrated luminosity. Results from the BDT analysis are shown with cuts that give similar signal to background ratio as the cut-based analysis.

| | | | | | Background fraction | | | |
|---|---|---|---|---|---|---|---|---|
| Modes | BDT Cut | Eff$_{WW}$(%) | $N_{WW}$ | $N_{bkg}$ | $t\bar{t}$ | $W^\pm Z$ | $Z+X$ | $N_{WW}/N_{bkg}$ |
| $e\nu\mu\nu$ | 200 | 39.6 | 419.9± 3.5 | 76.9± 6.0 | 47.7% | 27.8% | 21.8% | 5.46 |
| $\mu\nu\mu\nu$ | 290 | 15.5 | 90.3± 1.6 | 20.0± 2.8 | 54.1% | 34.6% | 11.3% | 4.53 |
| $e\nu e\nu$ | 240 | 15.9 | 60.5± 1.4 | 13.3± 2.8 | 81.4% | 7.2% | 11.4% | 4.54 |

### 3.6 $Z\gamma \rightarrow \ell^+\ell^-\gamma$ selection

$Z\gamma$ signals are produced through initial state radiation (ISR) of photon from the quarks as illustrated by the $t$- and $u$-channel diagrams shown in Figure 1. One of the goals is to measure the cross section of this $Z + \mathrm{ISR}\gamma$ production. The $s$-channel $Z\gamma$ production contains the $ZVV$ ($V = Z, \gamma$) vertex, which is

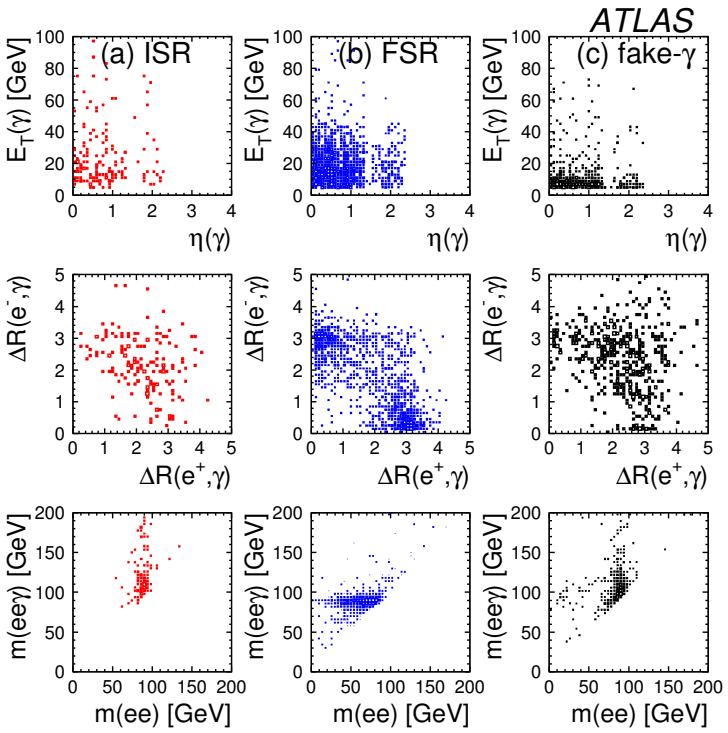


Figure 5: Distributions of $Z(ee)\gamma$ event variables for ISR (left column), FSR (middle col.) and fake photons (right col.).

forbidden at tree-level in the SM. Anomalous $Z\gamma V$ couplings can be investigated through this channel by measuring the $E_T(\gamma)$ distribution, expecially at large values.

This analysis aims to identify "signal" events with $Z$ plus an ISR photon. The backgrounds to this $Z\gamma$ signal are: 1) $Z$ production with a FSR photon, 2) $Z$ production with a fake photon, and 3) a small contamination from $W+X$ production reconstructed as a $l^+l^-\gamma$ final state. Some of the event variables are shown in Figure 5.

Events are pre-selected with $E_T(\gamma) > 10$ GeV, a value chosen to be above the PYTHIA generator threshold and as low as is reasonably achievable by detector reconstruction. The FSR event rate is almost an order of magnitude higher than the ISR rate. Backgrounds with a Z boson and a fake photon are comparable to the $Z\gamma$ ISR photon rate.

The event selection is conducted with BDTs trained to separate $Z\gamma$ events of different photon types. The training is in two stages: first to identify the FSR photon events and then to distinguish ISR photon from Z events with fake photons. Separate BDT training is done for the electron and muon $Z$ decay channels.

The BDTs are trained with 19 variables in total. As one example, FSR photons can be identified from the opening angle from the nearest lepton. Fake photons originating from neutral mesons decaying to two photons can not be directly identified within limits of the spacial resolution provided by the ECAL segmentation. However, they are often accompanied by jet secondaries or underlying remnant particles. By counting the charged tracks in a neighborhood (a cone of 0.45 rad in this case), or summing their energies, parameters useful for differentiating background from isolated ISR photons can be formed.

With the chosen BDT cuts the signal selection efficiency is 67%, and the signal to background ratio is 2.0 and 1.8 for the electron and muon $Z$ decay channels, respectively. The estimated numbers of

Table 10: The number of $Z\gamma$ signal and background events after pre-selection and BDT selection is listed, for an integrated luminosity of 1 fb$^{-1}$. The signal and total background are then scaled to NLO cross sections with the k-factors indicated.

| | | Signal | Background | | | |
|---|---|---|---|---|---|---|
| | | $Z\gamma$ | Z+FSR_$\gamma$ | Z+fake_$\gamma$ | $W(l\nu)\gamma$ | Total |
| $\ell = e$ | Pre-selected | 430 | 490 | 44 | 430 | |
| | BDT selection | 288 | 70 | 74 | 0 | |
| | NLO scaled | 337 (k=1.17) | | | | 187 (k=1.3) |
| $\ell = \mu$ | Pre-selected | 949 | 790 | 930 | 950 | |
| | BDT selection | 636 | 173 | 186 | 0 | |
| | NLO scaled | 774 (k=1.17) | | | | 467 (k=1.3) |

reconstructed $Z\gamma$ candidates for an integrated luminosity of 1 fb$^{-1}$ are listed in Table 10.

The FSR and fake photons contribute approximately equally to the total background but have important distinctions. The fake photons populate the low $E_T(\gamma)$ region, and are differentiated from the ISR in the $E_T(\gamma) \sim 20$ GeV region. The shape of the $E_T$ distribution in the low energy region is important for calibration and measurement of the production cross section with ISR photons. On the other hand, the FSR photons have an $E_T(\gamma)$ distribution similar to ISR photons which carry signatures of the coupling to the colliding quarks. Event rates in the high $E_T(\gamma)$ region, where the background is primarily FSR, is an important probe of new physics phenomenon.

### 3.7 $ZZ \to \ell^+\ell^-\ell^+\ell^-$ selection

The cleanest experimental signature for $ZZ$ detection is through the four lepton decay channels:

$$pp \to ZZ \to e^+e^-e^+e^-,\ \ \mu^+\mu^-\mu^+\mu^-,\ \ \ e^+e^-\mu^+\mu^-.$$

The $ZZ \to 4\ell'$ $(\ell' = e,\ \mu,\ \tau)$ signal is modeled by the PYTHIA LO event generator using the CTEQ6L PDF. The $Z/\gamma^*$ interference terms are included in the generator. With the 12 GeV mass cut on the dileptons decay from $Z/\gamma^*$, the cross section times the dilepton decay branching ratio, $\sigma \times BR$ is 159 fb. 'Filter' is applied to the simulated data to pre-select four lepton ($e$ and $\mu$ only) events by requiring that the lepton transverse momenta must be greater than 5 GeV, and the lepton rapidity, $\eta_\ell$, must be in a range between -2.7 and 2.7. The overall filter efficiency is 0.219. The $\tau$ lepton contribution to the four lepton channels ($4e,\ 4\mu,\ 2e2\mu$) is less than 4% in the event sample after the filter. The fraction of the on-shell $ZZ$ events in the sample is about 73%. The next-to-leading-order (NLO) calculations give higher production cross sections. The k-factor is about 1.35 when both $Z$'s are on mass shell. However, when the $Z/\gamma^*$ are off the $Z$ mass shell, the k-factor varies from 1.15 to 1.52 for the $Z/\gamma^*Z/\gamma^*$ mass range from 115 GeV to 405 GeV, which is determined by using the MCFM MC calculations [10]. The k-factor is set constant at 1.35 to normalize the $ZZ \to 4\ell$ signal events. The four-lepton events have high trigger efficiencies close to 100%.

Major background processes for four lepton final states are $t\bar{t} \to WWb\bar{b} \to 4\ell + X$ and $Zb\bar{b} \to 4\ell + X$. The $t\bar{t}$ background events, generated using *MC@NLO*, has a total production cross section of 833 pb. The $Zb\bar{b}$ background events, generated using *AcerMC*, has a production cross section of 52 pb. The k-factor is set to 1.42 to normalize the $Zb\bar{b}$ background.

Leptons from b-quark decays in these processes are produced in association with hadrons. Their contributions can be highly suppressed by lepton isolation requirements. For muons, the ratio between the transverse energy deposited in a cone around the muon track of radius $\Delta R = 0.4$ and the transverse

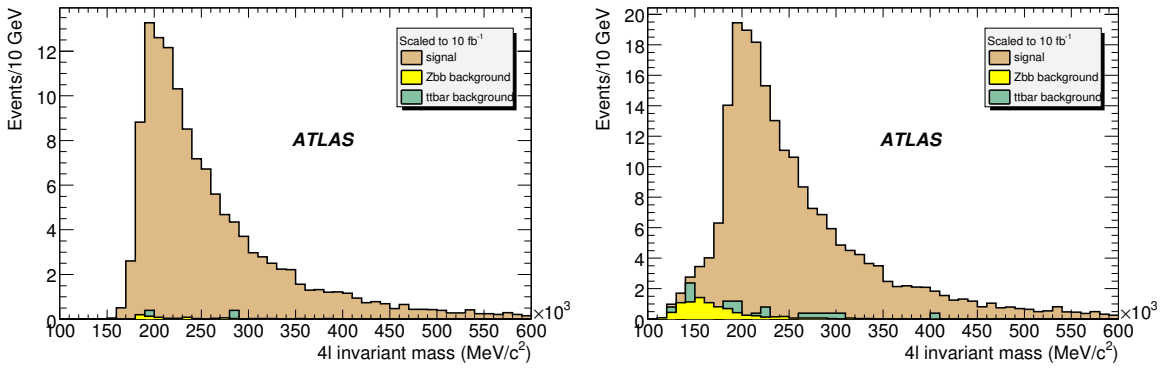


Figure 6: The 4-lepton invariant mass distributions of $ZZ$ signal, $Zb\bar{b}$ and $t\bar{t}$ background events with tight (left) and loose (right) Z mass cut on the lepton pairs.

energy of the muon $E_T^{\mu}$ must be below 0.2. A similar isolation cut is applied to electron selections. To reject background with leptons not originating from the $Z$ decays, the two opposite sign lepton pairs must have at least one lepton with $p_T$ greater than 20 GeV, and at least one lepton pair must have the invariant mass between 70 - 110 GeV. This is referred to as Loose Z mass cut. A Tight Z mass cut requires the second lepton pair to also have invariant mass between 70 - 110 GeV. The separation between the two leptons must have $\Delta R(\ell^+\ell^-)$ larger than 0.2. Table 11 lists the signal selection cut efficiencies for all the four lepton final states. Each cut efficiency value refers to the previous one and the product of the relative efficiencies agrees with the one obtained from the ratio of the number of events after cuts to the original number of generated events. The quoted uncertainties of the selected numbers of events are statistical only.

Table 11: Signal selection cut efficiencies

| | $4\mu$ [%] | | $4e$ [%] | | $2\mu 2e$ [%] | |
|---|---|---|---|---|---|---|
| Lepton Preselection | 70.67 | | 62.27 | | 65.40 | |
| Pair formation, dR | 99.34 | | 87.97 | | 93.37 | |
| Isolation, $p_T^{max}$ | 81.11 | | 58.62 | | 59.07 | |
| Z Mass | Tight | Loose | Tight | Loose | Tight | Loose |
| | 72.68 | 91.99 | 76.09 | 93.47 | 77.81 | 95.19 |
| Total | $41.39 \pm 0.64$ | $52.38 \pm 0.72$ | $24.43 \pm 0.50$ | $30.01 \pm 0.56$ | $28.07 \pm 0.37$ | $34.34 \pm 0.41$ |

The total selection efficiencies for the $Zb\bar{b}$ backround using these same tight cuts are $0.128\% \pm 0.064\%$, $0.606\% \pm 0.139\%$, and $0.510\% \pm 0.128\%$ for the $4\mu$, $4e$, and $2\mu 2e$ channels, respectively. For $t\bar{t}$ these efficiencies are $0.066\% \pm 0.066\%$ for all three channels. The expected number of signal and background events for $L = 1\text{fb}^{-1}$ requiring both on-shell Z's are given in Table 12. The expected signal and background events with only one on-shell Z (Loose $Z$ mass cut) are in Table 13. Uncertainties quoted in these tables are statistical only. Figure 6 shows the 4-lepton invariant mass distributions for the $ZZ$ signal, $Zb\bar{b}$ and $t\bar{t}$ background with tight and loose Z mass cut on the lepton pairs. Based on these results the ATLAS experiment will establish the $ZZ \to 4\ell$ signal with Poisson statistical significance of $7\sigma$ with the first 1 fb$^{-1}$ of integrated luminosity.

Table 12: Expected number of signal and background events at $L = 1$ fb$^{-1}$ using the tight $Z$ mass cut.

| | $4\mu$ events | $4e$ events | $2\mu 2e$ events | Total |
|---|---|---|---|---|
| Signal | 4.52±0.05 | 2.59±0.04 | 6.18±0.06 | 13.3 ±0.09 |
| $Zb\bar{b}$ | 0.009±0.003 | 0.042±0.007 | 0.035±0.006 | 0.076±0.010 |
| $t\bar{t}$ | 0.04±0.04 | 0.04±0.04 | 0.04±0.04 | 0.12±0.07 |
| Total bgr | 0.049±0.040 | 0.082±0.040 | 0.075±0.040 | 0.20±0.07 |

Table 13: Expected signal and background events at $L = 1$fb$^{-1}$ using the loose $Z$ mass cut.

| | $4\mu$ events | $4e$ events | $2\mu 2e$ events | Total |
|---|---|---|---|---|
| Signal | 5.72±0.06 | 3.17±0.04 | 7.56±0.07 | 16.5 ±0.10 |
| $Zb\bar{b}$ | 0.11±0.01 | 0.48±0.02 | 0.28±0.02 | 0.87±0.03 |
| $t\bar{t}$ | 0.08±0.06 | 0.52±0.14 | 0.44±0.13 | 1.03±0.20 |
| Total bgr | 0.19±0.06 | 1.00±0.14 | 0.72 ±0.13 | 1.90±0.20 |

### 3.8 $ZZ \to \ell^+\ell^-\nu\bar{\nu}$ selection

The $ZZ \to \ell^+\ell^-\nu\bar{\nu}$ signature is two high-$p_T$ leptons with a large missing transverse energy ($\not{E}_T$) due to the neutrino pair leaving the detector. The main backgrounds will either come from channels with large cross sections, such as $t\bar{t}$ and $Z \to \ell^+\ell^-$, or those with a similar signature to the signal, such as the $W^{\pm}Z$ diboson channel. Both signal ($ZZ \to \ell^+\ell^-\nu\bar{\nu}$) and background ($t\bar{t}$, $W^{\pm}Z$, $W^+W^-$, and DY dileptons) are modeled by the generator *MC@NLO*, except for high $p_T$ $Z$ ($p_T(Z) > 100$ *GeV*) events which are modeled by PYTHIA.

To reduce the backgrounds, a set of simple cuts on discriminating parameters is invoked. In general, each cut is used to suppress a particular background channel, as described below.

First, two oppositely charged good quality leptons with $p_T > 20$ GeV are selected. This reduces much of the $t\bar{t}$ background which contains softer leptons than the signal. This cut also reduces the background from $Z \to \tau^+\tau^- \to \ell^+\ell^-\nu_l\bar{\nu_l}\nu_\tau\bar{\nu_\tau}$ as the electrons and muons are produced with reduced $p_T$. The leptons must also lie within the inner detector pseudorapidity range, $|\eta| < 2.5$.

The lepton pairs are required to have an invariant mass close to the $Z$ mass, specifically $|m_{\ell\ell} - 91.2\text{ GeV}| < 10$ GeV. This is equivalent to $\sim 5\sigma$ of the signal width, and helps to reduce background combinatorics where the lepton pair does not come directly from a $Z$ decay. A lepton veto is imposed by combining the good quality and loose lepton selection to remove any events with more than two leptons in total. This reduces background from the $W^{\pm}Z$ channel, whose $Z$ has an almost identical signature to the signal, and the neutrino from $W$ decay also appears as $\not{E}_T$. The third-lepton veto suppresses the $W^{\pm}Z$ background by $\sim 30\%$. If the lepton from the $W$ is not reconstructed, however, this background channel becomes more problematic as it is almost indistinguishable from the signal.

A main characteristic of the signal decay is a large missing transverse energy ($\not{E}_T$) from the $Z \to \nu\bar{\nu}$ decay. An important background, due to its large cross section, comes from the $Z \to \ell^+\ell^-$ Drell-Yan process, where jets are produced in addition to the leptons. If these jets are aligned with cracks in the detector, then they will fake $\not{E}_T$ as they will not be fully accounted for in the calorimeters. This background can be significantly reduced by applying a 50 GeV $\not{E}_T$ cut. The background from $ZZ \to 4\ell$ is also reduced, but this is less significant as it has a much smaller cross section. The $W^{\pm}Z$ channel is suppressed by this cut as only one neutrino is produced, and hence the $\not{E}_T$ distribution is slightly softer.

The signal is expected to have missing $p_T$ equal and opposite to that of the reconstructed $Z$, assuming that the $ZZ$ pair is produced with no initial $p_T$ and that they decay back-to-back. Figure 7 (left and right)

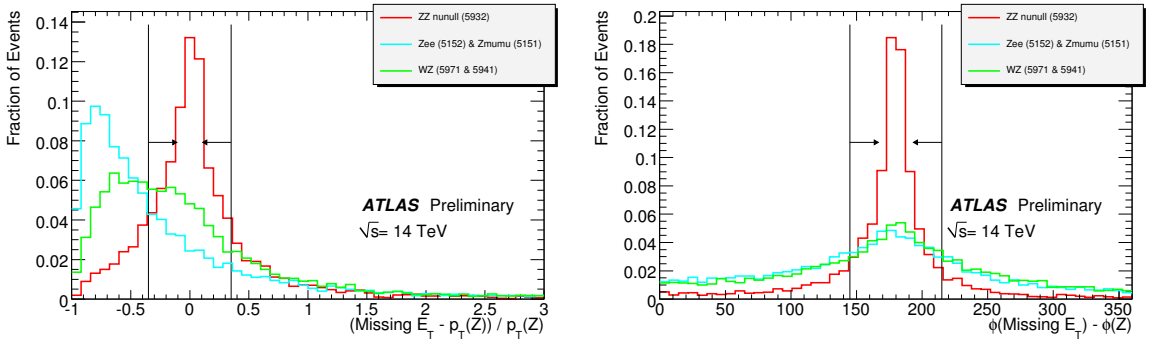


Figure 7: The $\not{E}_T - p_T(Z)$ magnitude and angle matching distributions before cuts for the signal (red), $ZZ \to 4\ell$ (orange), $Z \to \ell^+\ell^-$ (blue) and $W^\pm Z$ (green). The plots are normalised to unit area for comparison of distribution shapes.

shows a clear peak in the signal for both magnitude and angle matches. The $W^\pm Z$ background shows a worse magnitude match as some of the $W$ momentum is lost to either an electron or muon on decay. This means that the missing $p_T$ will not quite match up with that of the recoiling $Z$. The angular distribution shows a peak in both the $W^\pm Z$ and $Z \to ll$ channels. In the case of $W^\pm Z$, this is because the $W$ and $Z$ are produced in approximately opposite directions. When the $W$ decays, the neutrino will be deflected and so the peak has a wider distribution. In a similar way, in $Z \to ll$, the $Z$ is likely to be produced with some quarks recoiling against it. These will manifest themselves as jets which can fake $\not{E}_T$. Cuts at $(|\not{E}_T - p_T(Z)|)/p_T(Z) < 0.35$ and $145^\circ < \phi_Z - \phi_{\not{E}_T} < 215^\circ$, reduce the $W^\pm Z$ background.

A jet veto reduces backgrounds with large hadronic activity. For example, the predominant decay channel for the top quark in $t\bar{t}$ is the $t \to Wb$ final state, resulting in several high $p_T$ jets. Its contribution can be reduced by applying a veto on events containing any jet with $p_T(\text{jet}) > 30$ GeV and $|\eta_{\text{jet}}| < 3.0$.

The final cut to be applied is on the $p_T$ of the reconstructed $Z$ boson. This reduces the background from the single $Z$ channel, whose $p_T(Z)$ distribution drops much faster than the signal. A cut of $p_T(Z) > 100$ GeV significantly reduces this background, without harming the sensitivity to anomalous couplings, which only predominantly manifest at high $p_T$.

Using the single isolated electron trigger (effective $E_T > 25$ GeV) and the single isolated muon trigger (effective $p_T > 20$ GeV), the trigger efficiency for final $ZZ \to \ell^+\ell^-\nu\bar{\nu}$ events is expected to be 97%

Table 14 gives a summary of the cuts applied and present the expected number of events passing the cuts. Where simulated events remain after cuts, the final row in each column gives the statistical error. If zero events pass cuts, the figure given is the number of expected events at the 90% confidence level.

The expected sensitivity of the $ZZ \to \ell^+\ell^-\nu\bar{\nu}$ channel is summarised in table 15.

# 4 Cross section measurements

A binned likelihood method is used to determine the most likely cross sections. This likelihood method is also used to extract the sensitivities to the anomalous TGCs which will be described in Section 5. The likelihood is based on Poisson statistics convoluted with Gaussian probabilities to model the signal and background uncertainties. What follows is a more detailed description of the binned likelihood method followed by a description of the statistical and systematic uncertainties for the diboson cross section measurements using the first fb$^{-1}$ of data.

Table 14: Cut flow table for signal and background after cuts for an integrated luminosity of 1 fb$^{-1}$. The values in brackets indicate the percentage of events passing each cut relative to the previous cut.

| Cut | $ZZ \to \ell\ell\nu\nu$ | $ZZ \to 4l$ | $Z \to ll$ | $t\bar{t}$ | $W^{\pm}Z$ | $W^{+}W^{-}$ | $Z \to \tau\tau$ |
|---|---|---|---|---|---|---|---|
| Leptons | 130.1 | 54.3 | 13100 | 4530 | 271.2 | 491.1 | 2170 |
| Third-lepton veto | 101.9 | 3.1 | 1900 | 428.9 | 52.9 | 375.6 | 1690 |
| | (78.3%) | (5.7%) | (14.5%) | (9.5%) | (19.5%) | (76.5%) | (77.9%) |
| Di-lepton mass | 100.2 | 2.7 | 1740 | 110.2 | 45.3 | 83.8 | 40.1 |
| | (98.3%) | (87.1%) | (91.6%) | (25.7%) | (85.6%) | (22.3%) | (3.4%) |
| Missing $E_T$ | 38.0 | 0.34 | 3.8 | 17.9 | 9.4 | 18.3 | 0 |
| | (39.9%) | (12.6%) | (0.2%) | (16.2%) | (20.8%) | (21.8%) | (0.0%) |
| Jet veto | 34.4 | 0.30 | 0.44 | 6.0 | 7.6 | 16.7 | 0 |
| | (90.5%) | (88.2%) | (11.6%) | (33.5%) | (80.9%) | (91.3%) | (0.0%) |
| $p_T^Z$ | **10.2** | **0.08** | **0.4** | **3.0** | **1.7** | **0.02** | **0** |
| | (29.7%) | (26.7%) | (90.9%) | (50.0%) | (22.4%) | (0.1%) | (0.0%) |
| Stat. Error (90% CL) | 0.2 | 0.01 | 0.2 | 2.1 | 0.1 | 0.22 | (1.6) |

Table 15: Expected signal yields and sensitivity for 1 fb$^{-1}$ of integrated luminosity. The errors shown are statistical only.

| $N_{\text{signal}}$ | Signal efficiency | $N_{\text{background}}$ | $N_S/N_B$ | Significance |
|---|---|---|---|---|
| $10.2 \pm 0.2$ | 2.6% | $5.2 \pm 2.6$ | $2.0 \pm 0.8$ | 4.5 |

### 4.1 Binned likelihood

In the binned likehood method expected (determined from high statistics MC simulation) and observed (determined from MC simulation also for this work, but with appropriate statistical flutuation according to the luminosity) events are binned by one or more observables. As an example, in the case of the cross section measurement the BDT output spectrum, an example of which is shown in Figure 8, could be used. In the TGC analysis described in Section 5 the $M_T(VV)$ and $p_T(V)$ spectra are choosen.

For each bin expected signal and background are compared to the observed number of events ($n$ events in the bin) with a likelihood, which is based on Poisson statistics. We assume the systematic errors of the signal and background are Gaussian and uncorrelated for each bin. Thus, two Gaussian distributions are convolved with the Poisson distribution to form the likelihood

$$L = \int_{1-3\sigma_b}^{1+3\sigma_b} \int_{1-3\sigma_s}^{1+3\sigma_s} g_s\, g_b\, \frac{(f_s\nu_s + f_b\nu_b)^n\, e^{-(f_s\nu_s+f_b\nu_b)}}{n!}\, d f_s\, d f_b \quad \text{with} \quad g_i = \frac{e^{(1-f_i)^2/2\sigma_i^2}}{\int_0^\infty e^{(1-f_i)^2/2\sigma_i^2}}\ (i = s,b),$$

here the total systematic uncertainty of signal and background appear as $\sigma_s$ and $\sigma_b$, respectively.

From these likelihoods a total log-likelihood is formed from all the bin likelihoods. Some processes may also be separated into multiple channels (such as the three decay combinations of $WW \to ee, e\mu, \mu\mu$). Also, a factor of -2 is included to make this test statistic comparable to a chi-squared distribution. Thus, the negative log likelihood is

$$LL = -2 \sum_{k=\text{channels}} \sum_{i=\text{bins}} \log(L_i^k).$$

In cross section measurements, the likelihood is determined as a function of cross section in each 'bin' of a measured spectrum for each channel (e.g. the BDT output spectrum for the $W^+W^- \to e\nu\mu\nu$ channel as

shown on the left in Figure 8). The log likelihoods are then combined and the minimum of the negative log likelihood determines the most likely cross section (or anomalous TGC). The 68% C.L. limits ($\pm 1\sigma$) are taken from the minimum of the negative Log-likelihood plus 1.0. To set the 95% confidence-level interval of the anomalous TGC limits, likelihood minimum+1.92 is taken when fitting one parameter, and the minimum+2.99 for a fit of two parameters (e.g. two independent anomalous couplings).

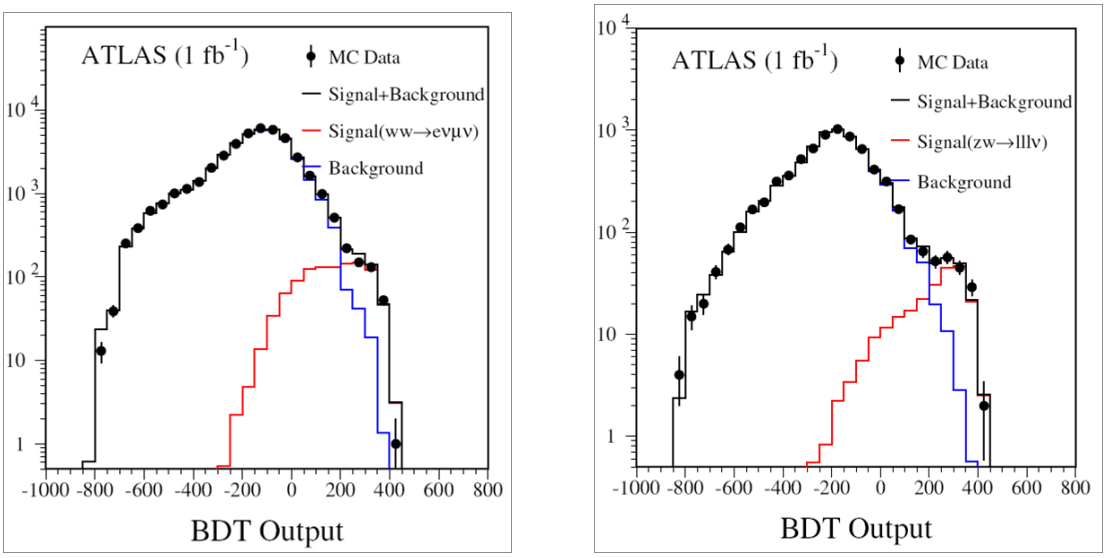


Figure 8: BDT-output spectra from a MC experiment for $W^+W^-$ (left) and $W^\pm Z$ (right) detection with 1 fb$^{-1}$. The dots in the plots are MC 'mock data'. The red histograms represent the 'signal' and the blue, 'background'.

### 4.2 Statistical uncertainties

Based on the diboson event selections described in Section 3, the expected number of signal and background events for 1 fb$^{-1}$ and the statistical significance of observing the Standard Model signals are summarized in Table 16, after taking into account the known background contributions. In the last column of the table the expected signal statistical uncertainties are also given. For 1 fb$^{-1}$ they range from 1.8% to 31.3% depending on the channel. For the BDT based analyses with 0.1 fb$^{-1}$ of data, the signal statistical errors are estimated to be 13% and 25% for $W^+W^-$ and $W^\pm Z$ detections, respectively. For $W^\pm\gamma$ and $Z\gamma$ detections the statistical errors should be less than 10% for 0.1 fb$^{-1}$ of data.

### 4.3 Systematic uncertainties

The major theoretical uncertainties on the production cross sections come from the PDF errors and the factorization scaling uncertainties (for NLO calculations). By varying the PDF's and scale values for $W^+W^-$, $W^\pm Z$, and $ZZ$ cross section calculations, the differences of the calculated cross sections are found to range from 3.4% to 6.2%.

The major experimental systematic effects in the cross section measurements arise from the uncertainties of the luminosity determination, the lepton identification efficiencies and energy/momentum resolutions, the jet energy scale and resolutions, and background model and estimate.

A promising possibility for the precise determination of the luminosity is to use the $W$ and $Z$ productions of single and pair leptons. The estimates show that in this way the luminosity errors could be

Table 16: Summary of signal and background of all diboson final states for 1 fb$^{-1}$ of integrated luminosity. The 4th column indicates the Poisson statistical significance, $N_\sigma$. The 5th column indicates the type of analysis and the overall signal selection efficiency, and the last column gives the signal statistical uncertainty. ($\ell$ denotes $e$ and $\mu$.)

| Diboson mode | Signal | Background | $N_\sigma$ | Analysis (signal eff.) | $\sigma_{stat}^{signal}$ |
|---|---|---|---|---|---|
| $W^+W^- \to e^\pm \nu \mu \mp \nu$ | $419.9 \pm 3.5$ | $80.8 \pm 8.0$ | 47 | BDT (eff=15.2%) | 4.9% |
| $W^+W^- \to \mu + \nu \mu^- \nu$ | $90.3 \pm 1.6$ | $20.2 \pm 2.8$ | 20 | BDT (eff=6.6%) | 10.5% |
| $W^+W^- \to e^+ \nu e^- \nu$ | $78.0 \pm 1.6$ | $35.4 \pm 3.6$ | 13 | BDT (eff=5.7%) | 11.3% |
| $W^+W^- \to \ell^+ \nu \ell^- \nu$ | $103.1 \pm 2.6$ | $16.6 \pm 2.0$ | 25 | Cut based (eff=2.0%) | 9.9% |
| $W^\pm Z \to \ell^\pm \nu \ell^+ \ell^-$ | $152.6 \pm 1.7$ | $16.1 \pm 2.5$ | 38 | BDT (eff=17.9%) | 8.1% |
| | $53.4 \pm 1.6$ | $8.0 \pm 1.1$ | 19 | Cut based (6.3%) | 13.7% |
| $ZZ \to 4\ell$ | $16.5 \pm 0.1$ | $1.9 \pm 0.2$ | 7.2 | Cut based (eff=7.7%) | 24.6% |
| $ZZ \to \ell^+ \ell^- \nu \bar{\nu}$ | $10.2 \pm 0.2$ | $5.2 \pm 2.0$ | 3.7 | Cut based (eff=2.6%) | 31.3% |
| $W\gamma \to e\nu\gamma$ | $1901 \pm 77$ | $1474 \pm 147$ | 50 | BDT (eff=6.7%) | 2.3% |
| $W\gamma \to \mu\nu\gamma$ | $2976 \pm 121$ | $2318 \pm 232$ | 62 | BDT (eff=10.5%) | 1.8% |
| $Z\gamma \to e^+ e^- \gamma$ | $337.4 \pm 12$ | $187.2 \pm 19$ | 25 | BDT (eff=5.5%) | 5.4% |
| $Z\gamma \to \mu^+ \mu^- \gamma$ | $774.8 \pm 25$ | $466.7 \pm 47$ | 36 | BDT (eff=12%) | 3.6% |

controlled to $\sim$5% [39]. It should be noted that a 6.5% luminosity uncertainty was quoted in Tevatron Run II early physics papers.

The lepton acceptance uncertainty is about 2-3% mainly due to the isolation requirement which involves the hadronic jet energy uncertainties. The lepton trigger efficiency uncertainties also contribute. With large $Z$ samples, this uncertainty could be minimized based on Tevatron experience. At the Tevatron, electron and muon ID efficiencies at the transverse momenta ($p_T$ ) typical of $W$ and $Z$ decay are measured reliably using leptons from $Z$ decay. $Z$ decays can typically be triggered and identified using only one of the two decay leptons. This leaves the second lepton unbiased from the point of view of trigger and offline identification. The rate at which the unbiased lepton passes the trigger and ID requirements provides a measurement of the respective efficiencies.

In the studies using the ATLAS simulated events the background estimate dominates the systematics with uncertainties of 15-25% for all the diboson channels except for the $ZZ \to \ell^+\ell^-\ell^+\ell^-$ channel, where the background uncertainty should be less than 2%. Even though more than 30 million fully simulated events are used to estimate the background, the analyses are still largely limited by $W + jets$ event sample statistics in the diboson background estimate. Tevatron experiments have used data to estimate the background, and typical uncertainties for diboson physics analyses are around 10% for 1 fb$^{-1}$ of data. With early LHC data (0.1 fb$^{-1}$), the background estimate uncertainty would be comparable to current Tevatron diboson background uncertainties, and with more data the uncertainties of the background estimate should decrease.

The lepton and jet energy resolution uncertainties will contribute to additional background estimate uncertainties which will further propagate to the cross section measurement errors. A study has been performed in $W^\pm Z$ analysis to estimate the size of such errors is given. In this study, the $W^\pm Z$ boosted-decision-trees are first trained with MC signal and background events simulated with the 'standard' detector energy resolutions and energy scale. For independent test samples, 10% and 3% are added to the jet and lepton energy resolutions, respectively, and the reconstructed energy related quantities are 'smeared' to reflect the uncertainties of the diboson detection sensitivity (signal to background ratio). In

Table 17: Change of background acceptance in a test of BDT ($W^{\pm}Z$ vs. $ZZ$) performed by smearing jet energy, $E_{jet}$, and missing $E_T$, $\not\!\!E_T$, by an additional 10%; and the lepton energy $E_T^{\ell}$ by an additional 3%.

| Signal Efficiency | Background Eff. No additional smearing | Background Eff. 10% for $E_{jet}$ & $\not\!\!E_T$ | Background Eff. 10% for $E_{jet}$& $\not\!\!E_T$, 3% for $E_T^{\ell}$ |
|---|---|---|---|
| 40% | 3.96% | 4.19% (+5.7%) | 4.23%(+6.7%) |
| 50% | 8.59% | 8.91% (+3.7%) | 9.00%(+4.8%) |
| 60% | 14.55% | 14.87% (+2.2%) | 15.08%(+3.7%) |
| 70% | 22.27% | 22.70% (+2.0%) | 23.02%(+3.4%) |

this study the signal efficiencies are fixed and changes to the background acceptance are gauged. The results are summarized in Table 17. As an example, for a BDT signal selection efficiency of 60%, the change of the signal to background ratio is 3.4%. For the $W^{\pm}Z$ cross section measurement with 1 fb$^{-1}$ of integrated luminosity, the 3.4-6.7% background contribution uncertainty would produce additional cross section measurement errors of about 2-3%.

### 4.4 Measurement errors vs. selection cuts and luminosities

The performance on cross section measurement errors versus the event selection cuts and the integrated luminosities are carried out in $W^+W^-$ and $W^{\pm}Z$ BDT based analysis. The BDT output spectra are used to build the Log-likelihood by using 'mock data', which is a sample of simulated events with appropriate statistics according to the luminosity and the Standard Model. For example, the BDT-output spectra for a MC experiment with 1 fb$^{-1}$ of data are shown in Figure 8 for $W^+W^- \to e^{\pm}\nu\mu^{\mp}\nu$ detection (left) and for $W^{\pm}Z \to \ell^{\pm}\nu\ell^+\ell^-$ detection (right). The Standard Model 'mock data' (dots) are compared to expected signal (red histogram) and background (blue histogram).

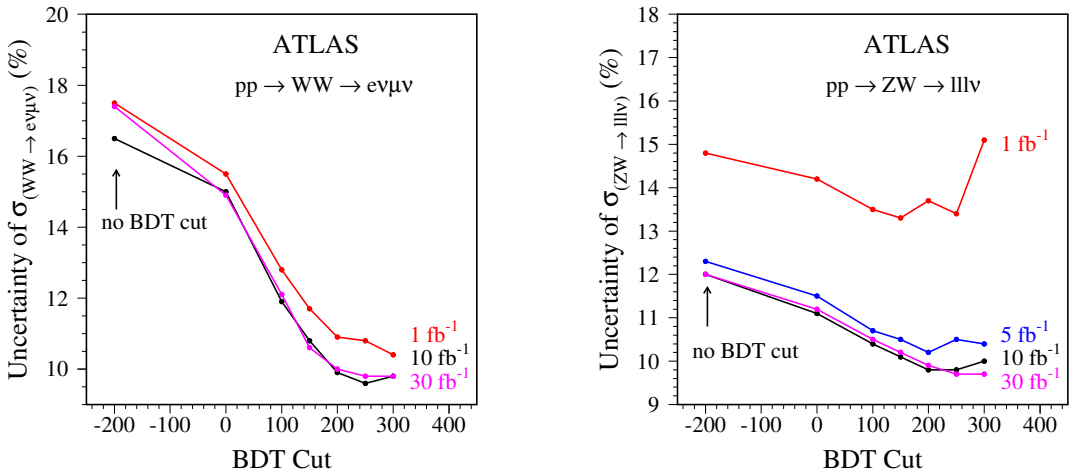


Figure 9: The relative errors for $W^+W^-$ (left) and for $W^{\pm}Z$ (right) cross section measurements as a function of the BDT cut for different luminosities. The optimal BDT cut is between 200 and 300. A total 9.2% systematical uncertainty was included in the fitting process.

To understand the optimal cut on the BDT spectra for cross section measurements, the cuts on the BDT spectra were varied and the cross section measurements by likelihood fittings were performed. A

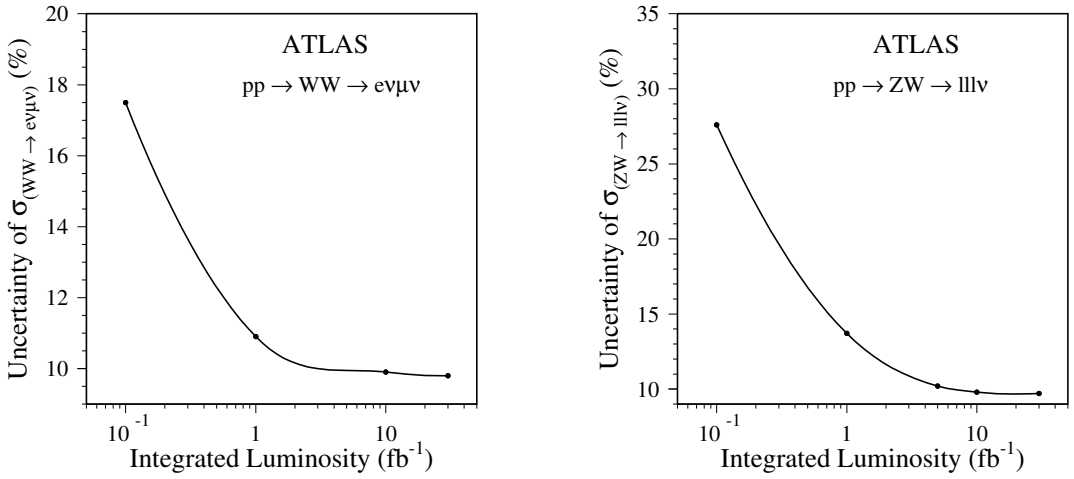


Figure 10: The $W^+W^-$ (left) and the $W^\pm Z$ (right) cross section measurement errors as a function of integrated luminosity (with BDT spectrum cut at 200). A total 9.2% systematical uncertainty was included in the fitting process.

total 9.2% systematical uncertainty was included in the fitting process. Figure 9 shows the cross section measurement error as a function of the BDT cut for different integrated luminosities from the $W^+W^-$ and the $W^\pm Z$ analysis.

Figure 10 shows the relative cross section errors as a function of integrated luminosity (with BDT spectrum cut at 200) for $W^+W^-$ (left) and $W^\pm Z$ (right) cross section measurements. From these plots it should be noted that the systematic error starts to dominate after 5 fb$^{-1}$ of integrated luminosity for $W^+W^-$ cross section measurements, and after 10 fb$^{-1}$ for $W^\pm Z$.

# 5 Sensitivity to anomalous couplings

The signature of anomalous couplings in diboson productions is an increase in the cross section at high values of gauge boson transverse momentum ($p_T$) and diboson transverse mass ($M_T$). The ATLAS sensitivity to anomalous TGC's is investigated by comparing the 'measured' diboson production cross sections and the vector boson $p_T$ or diboson $M_T$ distributions to models with anomalous TGC's. A binned likelihood fitting procedure using the $M_T$ or $p_T$ spectrum for each channel is followed to extract the 95% C.L. intervals of anomalous coupling parameters. The most dramatic effect is an increase in the high $M_T$ or high $p_T$ cross sections, so it is important to also include the overflow bin in the likelihood calculation. Details of the binned likelihood method are described in Section 4.1. One- and two-dimensional limits are set on the charged CP-conserving coupling parameters from the $W^+W^-$, $W^\pm Z$, and $W^\pm\gamma$ final states. The $ZZ$ final state is used to probe the neutral anomalous TGC sensitivity.

With non-Standard Model coupling parameters, the amplitudes for gauge boson pair production grow with energy, eventually violating tree-level unitarity. The unitarity violation is avoided by introducing an effective cutoff scale, $\Lambda$ [40]. The anomalous couplings take a form, for example,

$$\Delta\kappa(\hat{s}) = \frac{\Delta\kappa}{(1+\hat{s}/\Lambda^2)^n},$$

where $\sqrt{\hat{s}}$ is the invariant mass of the vector-boson pair and $\Delta\kappa$ is the coupling value in the low energy limit. The scale $\Lambda$ is physically interpreted as the mass scale where the new phenomenon, which

is responsible for the anomalous couplings, would be directly observable. $n = 2$ is used for charged anomalous TGC, and $n = 3$ for neutral anomalous TGC.

In order to compare results of this study to Tevatron's limits, $\Lambda$ values of 2-3TeV are used in the calculations. $\Lambda$ is physically interpreted as the mass scale with the new phenomenon which is responsible for the anomalous couplings would be directly observable. In principle, higher $\Lambda$ values comparable to the energy scale that can be reached by the LHC should be used to set the limits on the anomalous TGC's.

## 5.1 Re-weighting the fully simulated events

To avoid producing an impractically large number of fully simulated events in non-Standard Model anomalous coupling parameter space, a **re-weighting** method was invoked to study the ATLAS detector sensitivities to anomalous coupling parameters. The BHO and the BosoMC calculations are used with different anomalous coupling parameters to re-weight the fully simulated events generated by MC@NLO. As an example, Figure 11 shows the $W^+W^-$ production differential cross section distributions for Standard Model and some anomalous coupling parameters (left plot) and the corresponding differential cross section ratio, $d\sigma(\text{non-SM})/d\sigma(\text{SM})$ (right plot). These ratios have been used as *weights* to re-weight the fully simulated events to probe the anomalous TGC sensitivities. The *weights*

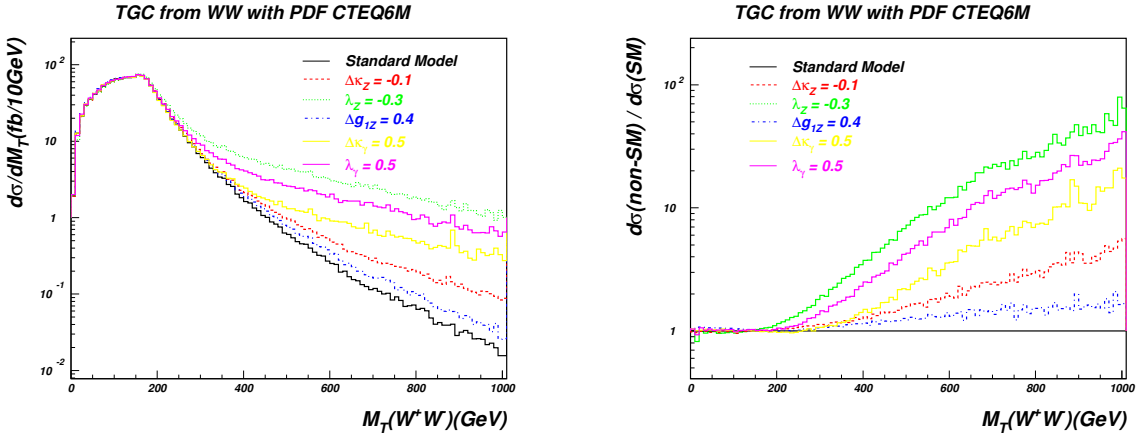


Figure 11: Left: WW transverse mass, $M_T$, distributions. Events are generated with the Standard Model coupling (black) and anomalous couplings (color); Right: the corresponding differential cross section ratio, $d\sigma(\text{non-SM})/d\sigma(\text{SM})$.

are generated in one-dimensional and two-dimensional anomalous coupling space according to parton level kinematics using the BHO and the BosoMC programs. To produce the weights the step size in coupling parameter space ranges from $0.1 \times 10^{-3}$ to $1.0 \times 10^{-3}$. For each point in the coupling parameter space 5M events were generated to obtain the theoretical 'reference' distributions. The fully simulated events with the Standard Model couplings are required to pass the events selection cuts, and then reweighted according to the generator level kinematics. The weighted events are equivalent to fully simulated events with the corresponding anomalous couplings. The distributions of variables, sensitive to the anomalous coupling, such as leption $p_T$, of the data event can be compared to those of simulated events with anomalous couplings included to extract the limits on the anomalous couplings. In this study the Standard Model 'mock data' are used to probe the ATLAS detector sensitivities to anomalous triple gauge boson couplings.

## 5.2 $WWZ$ anomalous TGC sensitivity in $W^{\pm}Z$ analysis

The $W^{\pm}Z$ diboson production involves exclusively the $WWZ$ coupling, in contrast to the $W^+W^-$ diboson final state which contains both $WWZ$ and $WW\gamma$ couplings. To extract the 95% C.L. sensitivity intervals of

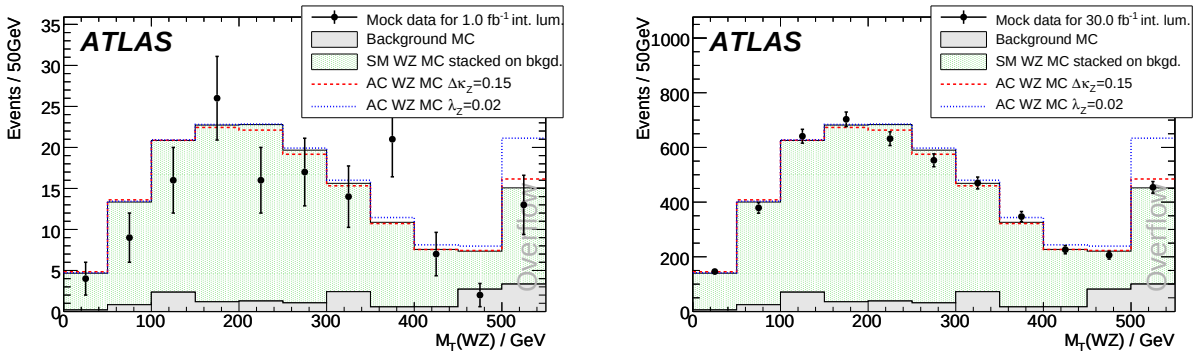


Figure 12: The expected signal+background of the Standard Model, superimposed with 'mock data' (points with error bars showing statistical uncertainty), and the non-Standard Model(anomalous couplings) predicted signal+background histograms (red and blue dashed lines). The left plot is for 1 fb$^{-1}$ of data and the right plot is for 30 fb$^{-1}$ of data.

Table 18: Summary of one-dimensional anomalous coupling parameter 95% CL sensitivities using the $M_T(W^{\pm}Z)$ fitting for $\Lambda = 2$ TeV and $\Lambda = 3$ TeV for integrated luminosities of 0.1, 1.0, 10.0 and 30.0 fb$^{-1}$.

| Int. Lumi (fb$^{-1}$) | Cutoff $\Lambda$ (TeV) | $\Delta\kappa_Z$ | $\lambda_Z$ | $\Delta g_1^Z$ |
|---|---|---|---|---|
| 0.1 | 2.0 | [-0.440, 0.609] | [-0.062, 0.056] | [-0.063, 0.119] |
| 1.0 | 2.0 | [-0.203, 0.339] | [-0.028, 0.024] | [-0.021, 0.054] |
| 10.0 | 2.0 | [-0.095, 0.222] | [-0.015, 0.013] | [-0.011, 0.034] |
| 30.0 | 2.0 | [-0.080, 0.169] | [-0.012, 0.008] | [-0.005, 0.023] |
| 0.1 | 3.0 | [-0.399, 0.547] | [-0.050, 0.046] | [-0.054, 0.094] |
| 1.0 | 3.0 | [-0.178, 0.281] | [-0.020, 0.018] | [-0.017, 0.038] |
| 10.0 | 3.0 | [-0.135, 0.201] | [-0.015, 0.013] | [-0.013, 0.018] |
| 30.0 | 3.0 | [-0.069, 0.131] | [-0.008, 0.005] | [-0.003, 0.016] |

the anomalous parameters, $\Delta\kappa_Z, \Delta g_1^Z$, and $\lambda_Z$, from the $W^{\pm}Z$ diboson final state, both the transverse mass of $W^{\pm}Z$ ($M_T(W^{\pm}Z)$) and the transverse momentum of Z ($p_T(Z)$) spectra are used to fit the anomalous couplings.

MC experiments are performed with 0.1, 1.0, 10, and 30 fb$^{-1}$ of integrated luminosities to study the anomalous coupling sensitivities. Figure 12 shows the expected signal+background of the Standard Model, superimposed with the 'mock data' (points with error bars), and the non-Standard Model (anomalous couplings) predicted signal+background distributions. Table 18 shows the summary of 1-dimensional 95% C.L. anomalous coupling parameter intervals based on the $M_T(W^{\pm}Z)$ spectra fitting. Results corresponding to 0.1, 1.0, 10.0 and 30.0 fb$^{-1}$ of integrated luminosities for cutoff, $\Lambda = 2$ TeV and $\Lambda = 3$ TeV are listed. It should be noted that even for 0.1 fb$^{-1}$ of integrated luminosity, the ATLAS sensitivity to $WWZ$ anomalous couplings could be much better (tighter) compared to Tevatron experiment limits based on 1 fb$^{-1}$ of $p\bar{p}$ collision data.

To understand the systematic error effects on the TGC sensitivity, three different systematic error assumptions are considered: (1) No systematic errors: $\sigma_S = 0$, and $\sigma_B = 0$; (2) Assume 7.2% (5% + 6.5% Lumi.) for signal, and 12% (10% + 6.5% lumi.) for background; and (3) 9.2% uncertainty for signal, and 18.3% uncertainty for background.

The 95% C.L. 1-dimensional limits for the $WWZ$ anomalous couplings, obtained from the fits to the $p_T(Z)$ assuming $\Lambda = 2$ TeV are shown in Table 19, for different scenarios of systematic errors. From this table it is seen that only when reaching 30 fb$^{-1}$ of integrated luminosity the systematic errors become significant enough to effect the TGC sensitivities.

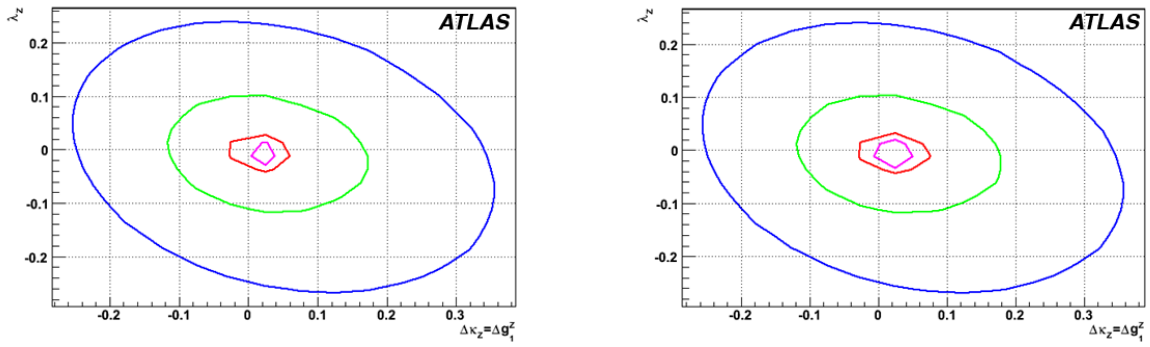


Figure 13: The left plot: 95% C.L. $WWZ$ TGC limit contour of $\lambda_Z$ vs. $\Delta\kappa_Z = \Delta g_1^Z$; without the systematic errors. The right plot: the 95% C.L. $WWZ$ TGC limit contour of $\lambda_Z$ vs. $\Delta\kappa_Z = \Delta g_1^Z$, with the systematic errors ($\sigma_S = 9.2\%,\ \sigma_B = 18.3\%$) included. The anomalous coupling limit contours from outer to inner corresponding integrated luminosities of 0.1, 1.0, 10.0 and 30.0 fb$^{-1}$, respectively. The systematic errors become significant when integrated luminosity reaching 30 fb$^{-1}$.

The studies on the $WWZ$ anomalous couplings in two-dimensional space are also based on the $p_T(Z)$ fits for different integrated luminosities (0.1, 1.0, 10.0 and 30.0 fb$^{-1}$) and for two cutoff values, $\Lambda = 2$ TeV and 3 TeV. The anomalous coupling (AC) limit contours are not very sensitive to these cutoff values. The effects of different systematic errors on the 2-dimensional TGC sensitivity contour are shown in Figure 13. The left plot shows the 95% C.L. anomalous TGC limit contour of $\lambda_Z$ vs. $\Delta\kappa_Z = \Delta g_1^Z$ without systematic errors, and the right plot shows the 95% C.L. TGC limit contour with the systematic errors ($\sigma_S = 9.2\%,\ \sigma_B = 18.3\%$) included. Again, the systematic errors become significant when the integrated luminosity reaches 30 fb$^{-1}$.

### 5.3 $WW\gamma$ anomalous TGC sensitivity in $W^{\pm}\gamma$ analysis

The $W^{\pm}\gamma$ diboson production involves exclusively the $WW\gamma$ coupling. To extract the 95% C.L. sensitivity intervals of the anomalous parameters, $\Delta\kappa_\gamma$ , and $\lambda_\gamma$, from the $W^{\pm}\gamma$ diboson final state, the photon transeverse energy $E_T(\gamma)$ distribution is used to fit the anomalous couplings, with $\Lambda = 2$ TeV. The intervals are calculated for $W^{\pm}\gamma$ events of electron and muon decays channels separately.

Figure 14 shows an $E_T(\gamma)$ distribution from $W^{\pm}(\ell^{\pm}\nu)\gamma$ normalized to 1 fb$^{-1}$ of data. The signal expectations at LO and NLO are shown by the dashed and dotted lines on the left in Figure 14. On the right in Figure 14 is shown the 95% confidence contour in the $\lambda_\gamma$-$\Delta\kappa_\gamma$ parameter space for 1 fb$^{-1}$ of data. The 1-dimensional 95% C.L. intervals of $\lambda_\gamma$ and $\Delta\kappa_\gamma$ are listed in Table 20.

### 5.4 $WWZ$ and $WW\gamma$ anomalous TGC sensitivity in $W^+W^-$ analysis

The $M_T$ spectrum of $W^+W^-$ pair is fitted to obtain the $WWZ$ and $WW\gamma$ anomalous TGC sensitivity intervals at 95% confidence level. A comparison of the $M_T(WW)$ distribution of the 'mock data' to that of models with anomalous coupling is shown in Figure 15. Five anomalous coupling parameters, ($\Delta\kappa_Z,\ \lambda_Z,\ \Delta g_1^Z,\ \Delta\kappa_\gamma,\ \lambda_\gamma$), have been studied with only one parameter varied at the time; the remaining parameters are fixed to Standard Model values. One dimensional anomalous coupling sensitivity intervals at 95%

Table 19: Comparison of one-dimensional anomalous coupling parameter 95% C.L. sensitivities for different systematic errors. Results obtained in this table are using the $p_T(Z)$ fit for $\Lambda = 2$ TeV and $\Lambda = 3$ TeV for integrated luminosities of 0.1, 1.0, 10 and 30 fb$^{-1}$.

| Systematic errors | Int. Lumi (fb$^{-1}$) | Cutoff $\Lambda$ (TeV) | $\Delta\kappa_Z$ | $\lambda_Z$ | $\Delta g_1^Z$ |
|---|---|---|---|---|---|
| $\sigma_S = 0$ | 0.1 | 2.0 | [-0.942, 1.130] | [-0.203, 0.193] | [-0.227, 0.324] |
| $\sigma_B = 0$ | 1.0 | 2.0 | [-0.561, 0.664] | [-0.093, 0.082] | [-0.106, 0.154] |
| | 10.0 | 2.0 | [-0.233, 0.231] | [-0.033, 0.024] | [-0.025, 0.061] |
| | 30.0 | 2.0 | [-0.128, 0.136] | [-0.024, 0.013] | [-0.009, 0.047] |
| $\sigma_S = 7.2\%$ | 0.1 | 3.0 | [-0.950, 1.140] | [-0.204, 0.194] | [-0.228, 0.325] |
| $\sigma_B = 12.0\%$ | 1.0 | 3.0 | [-0.574, 0.692] | [-0.093, 0.083] | [-0.106, 0.158] |
| | 10.0 | 2.0 | [-0.228, 0.302] | [-0.033, 0.027] | [-0.022, 0.070] |
| | 30.0 | 2.0 | [-0.164, 0.212] | [-0.026, 0.018] | [-0.009, 0.055] |
| $\sigma_S = 9.2\%$ | 0.1 | 3.0 | [-0.956, 1.150] | [-0.204, 0.194] | [-0.229, 0.326] |
| $\sigma_B = 18.3\%$ | 1.0 | 3.0 | [-0.583, 0.706] | [-0.094, 0.084] | [-0.106, 0.159] |
| | 10.0 | 2.0 | [-0.241, 0.316] | [-0.033, 0.028] | [-0.024, 0.071] |
| | 30.0 | 2.0 | [-0.184, 0.228] | [-0.028, 0.020] | [-0.011, 0.056] |

C.L. for different integrated luminosities are given in Table 21. The cutoff $\Lambda = 2$ TeV is used in these calculations.

The two-dimensional AC limits from $W^+W^-$ production with different scenarios relating the anomalous coupling parameters have also been investigated in this study.

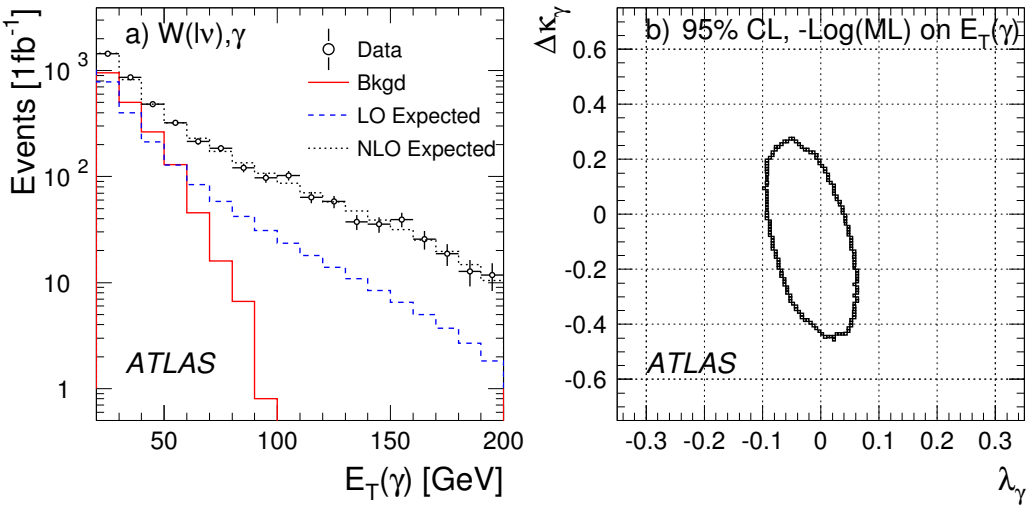


Figure 14: Left: the $E_T(\gamma)$ distributions of combined $W(e\nu)\gamma$ and $W(\mu\nu)\gamma$ sample for 1 fb$^{-1}$ of data. Right: the 95 % confidence contour in the $\lambda_\gamma$-$\Delta\kappa_\gamma$ parameter space for 1 fb$^{-1}$ of data. $\Lambda = 2$ TeV is assumed.

Table 20: 95% C.L. intervals for the anomalous $WW\gamma$ coupling parameters obtained from fitting the $E_T(\gamma)$ distribution to the NLO expectations using the combined sample of $W(e\nu)\gamma$ and $W(\mu\nu)\gamma$ events, with $\Lambda = 2$ TeV.

| | $W(\ell\nu)+ISR\gamma$ | | |
|---|---|---|---|
| | 1 fb$^{-1}$ | 10 fb$^{-1}$ | 30 fb$^{-1}$ |
| $\lambda_\gamma$ | [-0.09, 0.04] | [-0.05, 0.02] | [-0.02,0.01] |
| $\Delta\kappa_\gamma$ | [-0.43, 0.20] | [-0.26, 0.07] | [-0.11,0.05] |

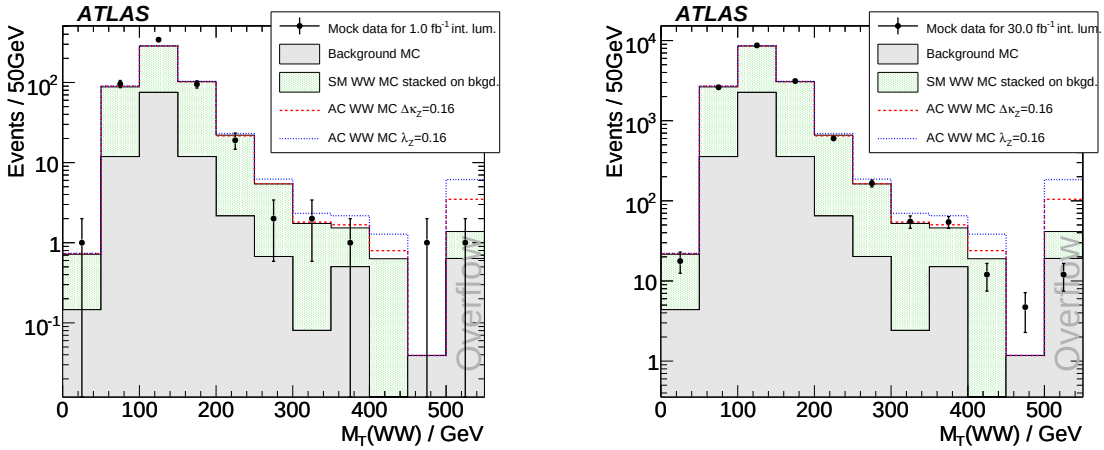


Figure 15: $W^+W^-$ transverse mass distributions for 1 (left) and 30 (right) fb$^{-1}$ of integrated luminosities. The last bins in the plots are 'overflow'-bins.

### 5.5 $ZZZ$ and $ZZ\gamma$ anomalous TGC sensitivity in $ZZ$ analysis

Measurements of the $pp \to ZZ$ differential cross section can be used to measure, or set limits on, $ZZZ$ and $ZZ\gamma$ couplings. These couplings are zero at tree level in the Standard Model.

Measurements of the couplings provide a sensitive test of the Standard Model, and non-zero values would indicate the presence of new physics beyond the Standard Model.

In order to estimate limits on anomalous couplings which may be obtained from measurements of $ZZ$ production in early ATLAS data, the $p_T$ distribution of the $Z$ boson is considered. In the $ZZ \to \ell\ell\nu\nu$ channel the visible $Z$ boson reconstructed from the charged leptons is used. In the $ZZ \to \ell\ell\ell\ell$ channel one of the two reconstructed $Z$ bosons is chosen in each event at random. Simulated 'mock data' distributions are fitted with the sum of expected signal and background distributions, where the signal distribution

Table 21: One-dimensional 95% C.L. interval of the anomalous coupling sensitivities from the WW final state analysis for 0.1, 1.0, 10.0 and 30.0 integrated luminosities, with $\Lambda = 2$ TeV.

| Lum. (fb$^{-1}$) | $\Delta\kappa_Z$ | $\lambda_Z$ | $\Delta g_1^Z$ | $\Delta\kappa_\gamma$ | $\lambda_\gamma$ |
|---|---|---|---|---|---|
| 0.1 | [-0.242, 0.356] | [-0.206, 0.225] | [-0.741, 1.177] | [-0.476, 0.512] | [-0.564, 0.775] |
| 1.0 | [-0.117, 0.187] | [-0.108, 0.111] | [-0.355, 0.616] | [-0.240, 0.251] | [-0.259, 0.421] |
| 10.0 | [-0.035, 0.072] | [-0.040, 0.038] | [-0.149, 0.309] | [-0.088, 0.089] | [-0.074, 0.165] |
| 30.0 | [-0.026, 0.048] | [-0.028, 0.027] | [-0.149, 0.251] | [-0.056, 0.054] | [-0.052, 0.100] |

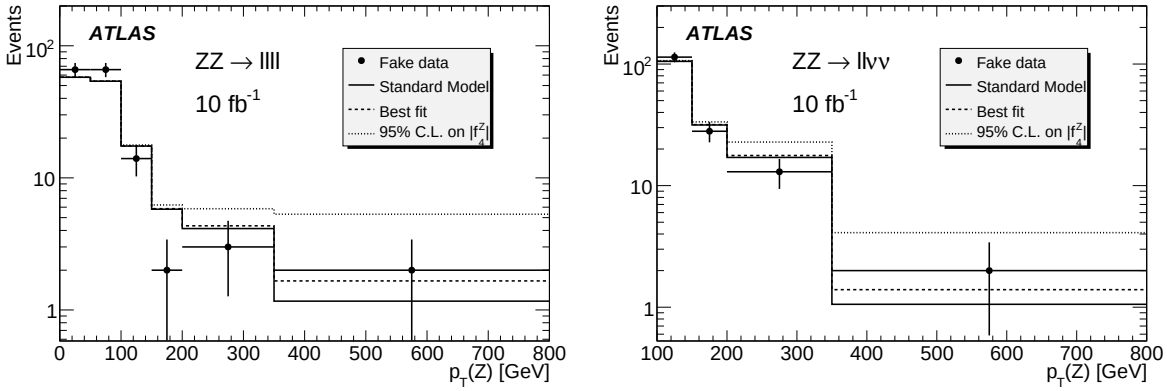


Figure 16: Example of a fit to one 'mock data' sample in each channel. The points show the total number of data events in each bin (not number per unit $p_T$ ). The histograms show the Standard Model prediction (solid), the best fit (dashed) and the 95% C.L. limit on $|f_4^Z|$ (dotted).

depends on the anomalous couplings. A binned maximum likelihood fit is employed, with systematic errors included by convolution with the predictions. Fits are performed to each channel separately, and a combined fit is performed by multiplying together the likelihoods from the two channels assuming no correlated errors.

Table 22: Expected 95% C.L. intervals on anomalous couplings from fits to the $ZZ \to \ell\ell\ell\ell$ channel, the $ZZ \to \ell\ell\nu\nu$ channel and both channels together for various values of integrated luminosity, with $\Lambda = 2$ TeV. In each case, other anomalous couplings are assumed to be zero.

| | L / fb$^{-1}$ | $f_4^Z$ | $f_5^Z$ | $f_4^\gamma$ | $f_5^\gamma$ |
|---|---|---|---|---|---|
| $ZZ \to \ell\ell\ell\ell$ | 1 | [–0.023, 0.023] | [–0.024, 0.024] | [–0.028, 0.028] | [–0.029, 0.028] |
| | 10 | [–0.010, 0.010] | [–0.010, 0.010] | [–0.012, 0.012] | [–0.013, 0.012] |
| | 30 | [–0.008, 0.008] | [–0.008, 0.008] | [–0.009, 0.009] | [–0.009, 0.009] |
| $ZZ \to \ell\ell\nu\nu$ | 1 | [–0.024, 0.024] | [–0.024, 0.025] | [–0.029, 0.029] | [–0.030, 0.029] |
| | 10 | [–0.012, 0.012] | [–0.012, 0.012] | [–0.014, 0.014] | [–0.015, 0.014] |
| | 30 | [–0.009, 0.009] | [–0.009, 0.009] | [–0.011, 0.011] | [–0.011, 0.011] |
| Combined | 1 | [–0.018, 0.018] | [–0.018, 0.019] | [–0.022, 0.022] | [–0.022, 0.022] |
| | 10 | [–0.009, 0.009] | [–0.009, 0.009] | [–0.010, 0.010] | [–0.011, 0.010] |
| | 30 | [–0.006, 0.006] | [–0.006, 0.007] | [–0.008, 0.008] | [–0.008, 0.008] |

An example fit for each channel is shown in Figure 16. The results presented here use four $p_T$ bins for the $\ell\ell\nu\nu$ channel and six $p_T$ bins for the 4-lepton channel, as shown in Figure 16. Reasonable modifications to the number or position of $p_T$ bins change the expected limits by up to 15% (12%) in the $\ell\ell\nu\nu$ ($\ell\ell\ell\ell$) channel. Removing the first two $p_T$ bins for the $\ell\ell\ell\ell$ channel, and fitting only the region $p_T > 100$ GeV has a negligible effect on the limits.

Table 22 shows the mean expected limits from each channel separately, and from combining the channels, for various values of integrated luminosity. With an integrated luminosity of 1 fb$^{-1}$ the sensitivities of the two channels are very similar. At higher luminosities, the $\ell\ell\ell\ell$ channel becomes somewhat more sensitive, because it has lower background and hence a lower associated systematic error. With as little as 1 fb$^{-1}$ of data it should be possible to improve the LEP limits [30] on $f_4^Z$, $f_5^Z$ and $f_5^\gamma$ by an order

of magnitude using a single channel, while a similar improvement on $f_4^\gamma$ will require both channels.

At an integrated luminosity of 10 fb$^{-1}$, the expected limits have only a low sensitivity to the background level and to the systematic errors. With the same signal efficiency but no background, the limits from the $\ell\ell\nu\nu$ channel improve by 10%, while those from the $\ell\ell\ell\ell$ channel change by only $\sim$0.2%; in the latter case, doubling the background has an effect of only $\sim$0.4%. Reducing all systematic errors to zero improves the limits by 7% (6%) in the $\ell\ell\nu\nu$ ($\ell\ell\ell\ell$) channel. Thus, the background level and systematic errors are unlikely to be important factors in obtaining limits from early data.

As discussed above, the expected limits are affected by the choice of $p_T$ bins. The number of bins is currently limited by the statistics of the fully simulated Monte Carlo events. Future studies would benefit from increased signal Monte Carlo statistics, particularly in the high $p_T$ region. In addition, samples of fully simulated events with anomalous couplings should be used to investigate the dependence of the efficiency at a particular $p_T$ value on the production diagram.

# 6 Summary

This note presents studies of the production of $W^+W^-$, $W^\pm Z^0$, $Z^0Z^0$,$W^\pm\gamma$ and $Z^0\gamma$ dibosons from pp collisions at the LHC, using leptonic decays of $W^\pm$ and $Z^0$ bosons. The simulated measurements are done using the ATLAS detector with full detector simulation and event reconstruction, and the statistics expected in the initial data taking periods. It concludes that Standard Model signals of $W^+W^-$, $W^\pm Z^0$, $W^\pm\gamma$ and $Z^0\gamma$ can be established with a statistical significance better than 5 sigma using the first 0.1 fb$^{-1}$ of integrated luminosity. $Z^0Z^0$ production can be established with 1 fb$^{-1}$ of data, using the four-lepton and the dilepton plus neutrino-pair decay channels. Table 16 lists the expected numbers of signal and background events using 1 fb$^{-1}$ of data, and the statistical significance of the Standard Model signals after taking into account the known background contributions.

Any significant deviation from the Standard Model prediction for these final states can lead to indications of new physics phenomena. In Section 6, the sensitivities to anomalous TGC are presented. The sensitivities are expressed in terms of constraints on the anomalous triple gauge boson couplings in the effective Lagrangian. Table 23 compares the 95% confidence level sensitivity interval for charged anomalous TGC's using observables from different diboson final states with 10 fb$^{-1}$ of integrated luminosity.

Table 23: 95% C.L. interval of the anomalous coupling sensitivities from $W^+W^-$, $W^\pm Z^0$, $W^\pm\gamma$ final states with 10.0 fb$^{-1}$ of integrated luminosity and the cutoff $\Lambda = 2$TeV. The table also indicates the variables used in the fit to set the AC sensitivity interval. For comparison, some recently published limits from Tevatron and LEP are also listed.

| Diboson, (fit spectra) | $\lambda_Z$ | $\Delta\kappa_Z$ | $\Delta g_1^Z$ | $\Delta\kappa_\gamma$ | $\lambda_\gamma$ |
|---|---|---|---|---|---|
| WZ, ($M_T$) | [-0.015, 0.013] | [-0.095, 0.222] | [-0.011, 0.035] | | |
| $W\gamma$, ($p_T^\gamma$) | | | | [-0.26, 0.07] | [-0.05, 0.02] |
| WW, ($M_T$) | [-0.040, 0.038] | [-0.035, 0.073] | [-0.149, 0.309] | [-0.088, 0.089] | [-0.074, 0.165] |
| $WZ$, (D0) ($1.0$fb$^{-1}$) | [-0.17, 0.21] | [-0.12, 0.29] | ($\Delta g_1^Z = \Delta\kappa_Z$) | | |
| $W^\pm\gamma$ (D0), ($0.16$fb$^{-1}$) | | | | [-0.88,0.96] | [-0.2,0.2] |
| $WW$, (LEP) | | | [-0.051,0.034] | [-0.105,0.069] | [-0.059,0.026] |
| ($\lambda_\gamma = \lambda_Z$,$\Delta\kappa_Z = \Delta g_1^Z - \Delta\kappa_\gamma \tan^2\theta_W$) | | | | | |

The neutral anomalous TGC's can be explored with the $Z^0\gamma$ and $Z^0Z^0$ final states. In this note, only $Z^0Z^0$ pair are used for constraining the anomalous coupling, with the study using $Z^0\gamma$ still in progress. Both the $Z^0Z^0 \to \ell^+\ell^-\ell^+\ell^-$ and $Z^0Z^0 \to \ell^+\ell^-\nu\bar{\nu}$ final states are used to constrain the neutral anomalous TGC parameters ( $f_4^Z$, $f_5^Z$, $f_4^\gamma$, $f_5^\gamma$ ). The 95% C.L. intervals on the anomalous couplings for 10 fb$^{-1}$ of integrated luminosity are listed in Table 24.

Table 24: Expected 95% C.L. intervals on anomalous couplings from fits to the $ZZ \to \ell\ell\ell\ell$ channel, the $ZZ \to \ell\ell\nu\nu$ channel and both channels together for 10 fb$^{-1}$ of integrated luminosity, with $\Lambda = 2$ TeV. In each case, other anomalous couplings are assumed to be zero. The 95% C.L. limits on MTGC from LEP ZZ detection are also listed.

| | $f_4^Z$ | $f_5^Z$ | $f_4^\gamma$ | $f_5^\gamma$ |
|---|---|---|---|---|
| $ZZ \to \ell\ell\ell\ell$ | [–0.010, 0.010] | [–0.010, 0.010] | [–0.012, 0.012] | [–0.013, 0.012] |
| $ZZ \to \ell\ell\nu\nu$ | [–0.012, 0.012] | [–0.012, 0.012] | [–0.014, 0.014] | [–0.015, 0.014] |
| Combined | [–0.009, 0.009] | [–0.009, 0.009] | [–0.010, 0.010] | [–0.011, 0.010] |
| LEP Limit | [–0.30, 0.30] | [–0.34, 0.38] | [–0.17, 0.19] | [–0.32, 0.36] |

The current status of the MC generators for diboson is less than satisfactory. *MC@NLO* is integrated with parton shower (Herwig), but it does not have matrix elements for the effective Lagrangian beyond the Standard Model with the anomalous couplings. The *BHO* MC program can generate parton-level LO and NLO diboson events with anomalous couplings, but can not be correctly integrated with the parton shower programs. In the current analysis, MC@NLO is used to simulate the Standard Model events. The *BHO* MC with anomalous TGCs is then used to re-weight the events so that the fully simulated events can effectively have the anomalous TGC's, and be used directly to compare with the simulated 'mock data'.

Compared to the previous ATLAS studies [3-8] which were all based on fast MC simulation of the detector, this study uses large data samples produced in recent years by much more realistic detector simulation and the full event reconstruction. It focuses on the sensitivities that ATLAS can achieve in the early running of LHC, rather than the ultimate sensitivites that ATLAS might reach after running at the design luminosity. The advanced analysis technique BDT is used in analysis of most of the final states, which improves the sensitivities significantly. As an example, the previous study of WZ final state [5] showed that with 30 fb$^{-1}$ of luminosity, the number of signal and background events are 1987 and 119 events. This analysis, using BDT, predicts 153 signal events and 16 background event at 1 fb$^{-1}$ of integrated luminosity. While BDT helps to improve the select efficiency, the more realistic simulation of Z+jets events increases the background level. Full simulation is essential to some of the signal channels, such as $ZZ \to \ell^+\ell^-\nu\bar{\nu}$, for which the previous fast simulation study [7] may have underestimated the background by an order of magnitude.

Because of the higher center of mass energy at the LHC, the cross sections for diboson production are an order of magnitude higher than that at the Tevatron. This will allow ATLAS to improve the Tevatron measurements in the early running of the LHC. The large signal statistical significances and signal to background ratios determined from these studies suggest that early observations of these channels will take place at the LHC start up with 0.1 to 1 fb$^{-1}$ of data. Systematical uncertainties will dominate the cross section measurement errors starting from 5-30 fb$^{-1}$ of data. With increasing luminosity, the constraints on the anomalous coupling will provide important probes of physics beyond the Standard Model.

## References


[1] S. Weinberg, Phys. Rev. Lett. 19, 1264 (1967);
A. Salam, p. 367 of Elementary Particle Theory, ed. N. Svartholm (Almquist and Wiksells, Stockholm, 1969);
S.L. Glashow, J. Iliopoulos, and L. Maiani, Phys. Rev. D2, 1285 (1970).

[2] J. Ellison and J. Wudka, Annu. Rev. Nucl. Part. Sci. 48, 33(1998).

[3] ATLAS Detector and Physics Performance, Technical Design Report. ATLAS TDR 15, CERN/LHCC 99-15.

[4] Proceedings of the Workshop on Standard Model Physics (and more) at the LHC, CERN Yellow Report, CERN 2000/004, May 2000, - 117p, editors: G.Altarelli and M.L.Mangano.

[5] M. Dobbs, M. Lefebvre, 'Prospects for probing the three gauge boson couplings in W + photon production at the LHC', ATL-PHYS-2002-022
'Prospects for probing the three gauge boson couplings in W + Z production at the LHC', ATL-PHYS-2002-023.

[6] S. Hassani, 'Prospect for measuring neutral gauge boson couplings in $Z\gamma$ production with the ATLAS detector', ATLAS-PHYS-2003-023.

[7] S. Hassani, 'Prospects for measuring neutral gauge boson couplings in ZZ production with the ATLAS detector', ATL-PHYS-2003-022.

[8] Lj. Simić *et al.* 'Prospects for Measuring Triple Gauge Boson Couplings in WW Production at the LHC', ATL-PHYS-2006-011, CERN 2006.

[9] Hai-Jun Yang et.al., Nucl. Instrum. & Meth. A **555** (2005) 370-385, [physics/0508045]; Nucl. Instrum. & Meth. A **543** (2005) 577-584, [physics/0408124]; Nucl. Instrum. & Meth. A **574** (2007) 342-349, [physics/0610276].

[10] J.M. Campbell and R.K. Ellis, Phys. Rev. D60, 113006(1999).

[11] L. Dixon, Z. Kunszt, A. Signer, Phys. Rev. D**60**, 114037(1999).

[12] J. Ohnemus, Phys. Rev. D**47**, 940(1993);
V. Barger, T. Han, D. Zeppenfeld, J. Ohnemus, Phys. Rev. D**41**, 2782(1990).

[13] http://projects.hepforge.org/lhapdf/pubs
J. Pumplin, D.R. Stump, J. Huston, H.L. Lai, P. Nadolsky, W.K. Tung,
'New Generation of Parton Distributions with Uncertainties from Global QCD Analysis', hep-ph/0201195.

[14] S. Frixione and B.R.Webber JHEP 0206 (2002) 029;
S. Frixione, P. Nason and B.R.Webber, JHEP 0308 (2003) 007.

[15] M. Dobbs, 'Probing the Three Gauge-boson Couplings in 14 TeV Proton-Proton Collisions', Ph. D. Thesis (2002), University of Victoria;
M. Dobbs, M. Lefebvre, 'Unweighted event generation in hadronic WZ production at the first order in QCD', ATL-PHYS-2000-028.

[16] U. Baur, T. Han and J. Ohnemus, Phys. Rev., D50, 1917 (1994) ;
U. Baur, T. Han and J. Ohnemus, Phys. Rev., D51, 3381 (1995) ;
U. Baur, T. Han and J. Ohnemus, Phys. Rev., D53, 1098 (1996) ;
U. Baur, T. Han and J. Ohnemus, Phys. Rev., D57, 2823 (1998) ;

[17] F. Larios, M. A. Perez, G. Tavares-Velasco, J. J. Toscano, Phys. Rev. D**63**, 113014(2001);
U. Baur and D. Zeppenfeld, Phys. Lett. B**201**, 383(1988);
Hagiwara K, P. Peccei, D. Zeppenfeld, Nucl. Physics B**282**, 253(1987).

[18] U. Baur, T. Han and J. Ohnemus, Phys. Rev. D**57**, 2823(1998);
G. J. Gounaris, J. Layssac, F. M. Rennard, Phys. Rev. D**62**, 073013(2000);
U. Baur, D. Rainwater, Phys. Rev. D**62**, 113011(2000);
M. A. Perez and F. Ramirez-Zavaleta, 'CP violation effects in the decay $Z \to \mu^+\mu^-\gamma$ induced by $ZZ\gamma$ and $Z\gamma\gamma$ couplings', hep-ph/0410212v4, 11 Jan. 2005.

[19] E. Lipeles, ' WW and WZ Production at the Tevatron', 33rd International Conference on High Energy Physics (ICHEP 06), Moscow, Russia, 26 Jul - 2 Aug 2006. arXiv:hep-ex/0701038 (2007).

[20] The DØ Collaboration, Phys. Rev. Lett. **94**, 151801 (2005).

[21] The CDF Collaboration, Phys. Rev. Lett. **98**, 161801 (2007).

[22] The DØ Collaboration, Phys. Rev. D **76**(2007).

[23] The CDF Collaboration, Phys. Rev. Lett. **94**, 041803 (2005).

[24] The DØ Collaboration, Phys. Lett. B**653**, 378(2007).

[25] The DØ Collaboration, Phys. Rev. D **71**, 091108 (2005).

[26] The CDF Collaboration, 'First Measurement of ZZ production in $p\bar{p}$ Collision at $\sqrt{s} = 1.96$ TeV', hep-ex/0801.4806 (2008).

[27] The DØ Collaboration, ' Search for $ZZ$ and $Z\gamma^*$ production in $p\bar{p}$ collisions at $\sqrt{s} = 1.96$ TeV and limits on anomalous $ZZZ$ and $ZZ\gamma^*$ couplings', submitted to Phys. Rev. Lett. hep-ex/0712.0599 (2007).

[28] The DØ Collaboration, Phys. Rev. D **74** 057101 (2006).

[29] The CDF Collaboration, Phys. Rev. D **76** 111103 (2007).

[30] D. Abbaneo *et al.*, ALEPH, DELPHI, L3, OPAL Collaborations and LEP Electroweak Working Group and SLD Heavy Flavor and Electroweak Group, CERN-EP-2001-098 [hep-ex/0112021];
Review of Particle Physics (PDG), p1098 (2004);
The LEP collaborations ALEPH, DELPHI, L3, OPAL and the LEP electroweak working group, *A Combination of Preliminary Electroweak Measurements and Constraints on the Standard Model*: CERN-PH-EP-2006-042, hep-ex/0612034, November 2006.

[31] http://hepwww.rl.ac.uk/theory/seymour/herwig/hw65_manual.htm

[32] T. Binoth, M. Ciccolini, N. Kauer and M. Kraemer, JHEP12, 046(2006).

[33] Sjostrand, T., *et al.*, Comput. Phys. Commun., **135**, 238259 (2001).

[34] M.L. Mangano, M. Moretti, F. Piccinini, R. Pittau and A. Polosa, JHEP 0307:001 (2003).

[35] G.Aad *et al.*, 'The ATLAS Experiment at the CERN Large Hadron Collider ', submitted to JINST.

[36] The MiniBooNE Collaboration, A.A. Aguilar-Arevalo et.al., Phys. Rev. Lett. **98**, 231801 (2007);
The BABAR Collaboration, B. Aubert et.al., [hep-ex/0607112];
The D0 Collaboration, V.M. Abazov et.al., Phys. Rev. Lett. **98** , 181802 (2007);
J. Bastos, [physics/0702041].

[37] Hai-Jun Yang et.al., [arXiv:0708.3635]; Accepted by JINST (2008) for publication.

[38] Particle Data Group: W.-M. Yao *et al.*, Journal of Physics, G **33**, 1 (2006).

[39] M. Dittmar, F. Pauss, D. Zuercher, Physi. Rev. D 56 (1997) 7284-7290.

[40] U. Baur, 'Selfcouplings of electroweak bosons: Theoretical aspects and tests at hadron colliders.' Europhysics Conf. on High Energy Physics, Brussels, Belgium, Jul 27-31, 1995. Published in Brussels EPS HEP 1995:197-200 (hep-ph/9510265)

[41] LEP Collaborations ALEPH, DELPHI, L3, OPAL and the LEP Electroweak Working Group, CERN-EP/2006-042,p.52, 2006; hep-ex/0612034.